vehicles

MDPI

Article

Prestressed Cable-Spring Joints as a Lightweight Reinforcement Strategy for Tubular Body Structures in Conventional and Autonomous Buses

Kostiantyn Holenko [1], Oleksandr Dykha [1], Marco Guerrieri [2,*] and Larysa Neduzha [3,*]

[1] Department of Tribology, Automobiles and Materials Science, Khmelnytskyi National University, 29016 Khmelnytskyi, Ukraine; holenkoke@khmnu.edu.ua (K.H.); duhaov@khmnu.edu.ua (O.D.)
[2] Department of Civil, Environmental and Mechanical Engineering (DICAM), University of Trento, Via Mesiano 77, 38123 Trento, Italy
[3] Department of Technical Mechanics, Ukrainian State University of Science and Technologies, Lazaryan 2, 49010 Dnipro, Ukraine
* Correspondence: marco.guerrieri@unitn.it (M.G.); nlorhen@i.ua (L.N.)

Abstract

Bus body structures are commonly reinforced by increasing the dimensions or number of steel members, resulting in higher vehicle mass and material consumption. This study proposes a lightweight reinforcement concept based on prestressed Cable Spring (CS) joints for tubular bus body structures. An analytical model describing the stiffness contribution of tension-only prestressed cables was developed and implemented in Ansys Mechanical. The concept was evaluated using finite-element models of the low-entry city bus body "4289" under two representative loading conditions: diagonal racking and inertial loading prescribed by UNECE Regulation No. 100 (R100). Under diagonal racking, the proposed CS system reduced the maximum von Mises stress by 2.7%, the average stress by 16.2%, and the maximum total deformation by 28.4%. Under the R100 transverse 5 g loading condition, the combined catenary-curved and CS configuration decreased the maximum equivalent stress, average stress, and maximum deformation by 41.2%, 24.7%, and 75.1%, respectively, relative to the conventional rectangular body frame. The results demonstrate that prestressed CS joints constitute an effective lightweight reinforcement strategy for improving the structural efficiency of tubular body structures of conventional and autonomous buses, with these benefits being primarily associated with reduced structural material use.

Keywords: tubular bus body; prestressed cable reinforcement; spring joint; catenary-curved body frame; racking stiffness; UNECE R100; passive safety; autonomous bus; Ansys Mechanical

Check for updates

Academic Editors: Muhammad Hussain, Xiaomeng Li, Paul Roberts and Amjad Pervez

Received: 23 August 2026
Revised: 23 September 2026
Accepted: 8 October 2026
Published: 11 October 2026

Copyright: © 2026 by the authors. Licensee MDPI, Basel, Switzerland. This article is an open access article distributed under the terms and conditions of the Creative Commons Attribution (CC BY) license.

1. Introduction

A modern transportation system is impossible without the operation of both conventional [1–3] and autonomous [4,5] vehicles. A vehicle is an important link in the safe and efficient functioning of this system [6,7]. All its components are subject to modern requirements throughout the design [8–11], testing [12–17], operation [18–21], monitoring [22–25], maintenance [26–30], and other stages. In particular: ensuring traffic safety [31–35], minimizing negative impact on the environment, implementing energy-saving technologies [36–39], increasing energy efficiency, improving and analyzing the dynamic behaviour of vehicles [40–44], ensuring reliable operation of the infrastructure [45–48], etc. This will con-

tribute to the development of new structures in all sectors of transport and their high-quality operation [49–53].

The demand for lighter, safer, and more energy-efficient public transport vehicles has become one of the principal driving forces in modern bus body engineering [54–57]. The same requirement applies to emerging autonomous and highly automated bus platforms, where roof-mounted sensor arrays and additional onboard equipment further increase the structural demands on the upper body section. Achieving a substantial reduction in structural mass while preserving stiffness, strength, durability, and regulatory crashworthiness remains a major unresolved challenge, particularly for tubular bus body structures produced by independent body manufacturers [58–60]. Despite the ongoing development of passenger vehicle structures [61–65], bus body engineering still retains several design principles inherited from the historical coachbuilding era [66–69]. Unlike passenger cars, where the chassis and body are generally developed as an integrated structure by a single manufacturer [70–73], many buses are still produced by independent body manufacturers who mount proprietary body structures onto commercially available chassis supplied by major OEMs such as Mercedes-Benz, MAN, Scania, Volvo, Iveco, DAF, or Isuzu. This manufacturing approach is particularly common among regional and small-scale bus builders, whose annual production typically ranges from several dozen to several hundred vehicles, depending on market segment and company size. Because the body structure accounts for approximately 35–45% of the total manufacturing cost of a bus (depending on its class and type), independent manufacturers continuously seek structural solutions that reduce material consumption while maintaining the required levels of stiffness, strength, durability, and passenger safety [74–77]. Consequently, bus body structures differ considerably in their geometric layout, passenger compartment configuration, structural topology, material selection and tubular cross-sections under diverse operating conditions [78–81]. These differences have resulted in distinctive structural design philosophies adopted by individual manufacturers, each representing a compromise between weight, manufacturing cost, crashworthiness and service life [82–85].

Increasing market competition places growing demands on lightweight yet stiff body structures, stimulating the development of unconventional structural concepts [86–91]. Previous studies by the present authors demonstrated that adopting a catenary-curved sidewall profile significantly improves the load-carrying behaviour of the body frame [92–94], while replacing conventional rectangular modules with triangulated structural layouts further increases overall stiffness [95–99]. Despite these advances, all existing approaches share a common characteristic: the hollow interiors of the structural tubes remain unused [100–103]. A further step toward improving the structural efficiency of bus bodies was proposed in [74,104], where the hollow inter-window pillars were utilized for integrating traction battery modules in a low-floor electric bus. Building on the same concept of exploiting the unused internal volume of tubular members, the present study proposes an alternative engineering solution. Prestressed steel cables (hereinafter referred to as Cable Spring (CS) joints) are installed within selected structural tubes wherever technologically feasible and anchored at both ends using turnbuckles, equivalent mechanical tensioning devices, or welding processes [105–109]. Additional diagonal CS joints may also be introduced to connect opposite corners of rectangular frame modules while remaining completely concealed beneath the interior body panels. The proposed CS joints are intended to redistribute internal forces within the body frame, thereby improving stress uniformity, increasing structural stiffness and suppressing local stress concentrations. The resulting increase in structural efficiency creates the potential to reduce the cross-sectional dimensions of the steel members and, consequently, the bus's curb weight without compromising structural safety. The effectiveness of the proposed concept is evaluated under

two representative loading conditions: diagonal racking, developed here as an extension of the beam-model approach of [110], and the inertial loading cases specified by UNECE Regulation No. 100 (hereinafter R100), whose application to the same bus body structure was initially investigated in [111].

Recent studies have demonstrated the effectiveness of prestressed and cable-based reinforcement in a range of structural systems. Gao et al. [112] investigated concrete frames strengthened with externally prestressed cables and showed that cable prestressing can improve load-carrying behaviour and modify the deformation response. Wang et al. [113] demonstrated that prestressed cable bracing can significantly enhance the global stability of spatial glulam gridshell structures, confirming the efficiency of tension-based reinforcement in lightweight spatial systems. From a durability perspective, Li et al. [114] reported fatigue fracture of stay-cable anchorage components associated with excessive cable vibration, highlighting the importance of cyclic cable-force variation, anchorage detailing, and inspection. Wu et al. [115] showed, through vehicle–bridge coupled analysis, that the dynamic response of cable-stayed structures is strongly influenced by vehicle-induced excitation and cable-force characteristics. He et al. [116] combined experimental testing and finite-element analysis to demonstrate the structural contribution of prestressed diagonal braces in a cable-stayed bridge system. Related recent transport-engineering studies have also emphasized the importance of integrated modelling of strongly coupled railway systems and the development of computationally efficient linearized approaches for complex vehicle–infrastructure interactions [117]. In a related field of tubular-structure manufacturing, recent work on spatial spiral-tube multi-roller bending has further shown that the final three-dimensional geometry of bent tubular members is strongly affected by forming-induced deformation and springback, which can be accurately predicted using combined finite-element and data-driven approaches [118].

Prestressed and cable-based reinforcement concepts have been widely investigated in civil and thin-walled structures, where tension elements can provide additional load paths, improve stiffness and stability, and facilitate load redistribution with a relatively small mass penalty. Recent studies have demonstrated the effectiveness of prestressed cables in thin-walled steel members and tubular steel elements, showing that cable stiffness, initial pretension, and spatial cable configuration can significantly influence structural stability and deformation behaviour [119,120]. Related investigations of lightweight spatial and steel-frame systems have further demonstrated that prestressed tension elements can redistribute internal forces and provide an alternative to conventional rigid bracing [121,122]. Fatigue and serviceability remain important design considerations for prestressed cable systems, particularly under cyclic vehicle-induced loading, where traffic excitation, road roughness, corrosion, cable-force variation, and local bending near anchorages may significantly influence cable life [123–125].

However, their application to spatial tubular vehicle bodies remains comparatively limited. In particular, the integration of concealed prestressed tension-only elements into hollow bus-body members, together with their influence on global racking stiffness, structural load redistribution, and serviceability, has not been sufficiently investigated. This gap is especially relevant for bus structures, where the effectiveness of reinforcement must be balanced against structural mass, packaging constraints, fatigue resistance, and long-term maintenance requirements.

The novelty of the present study lies not in the general principle of structural prestressing or in the catenary-curved and triangulated bus-body geometries investigated in the authors' previous studies, but in the implementation of concealed tension-only reinforcement within a spatial tubular bus body. In particular, prestressed CS joints are introduced into otherwise unused hollow structural members (or beyond them depending

on the configuration) and combined with catenary-curved inter-window pillars to form a bow–bowstring load-carrying system. This configuration provides additional load paths without introducing conventional rigid diagonal braces or substantially modifying the passenger-compartment layout.

2. Materials and Methods

This section presents the analytical formulation and finite-element methodology used to evaluate the structural effectiveness of the proposed prestressed Cable Spring (CS) reinforcement system. The investigation comprises the development of the cable-force and stiffness model, its implementation in Ansys Mechanical, and the definition of the loading and boundary conditions for the diagonal racking and UNECE R100 simulations.

2.1. Analytical Model of the Prestressed Cable-Reinforced Frame

To provide a simplified analytical representation of the proposed cable-reinforced bus body structure, a single rectangular frame cell reinforced by a prestressed diagonal cable is considered (Figure 1). The frame is characterized by its horizontal span L (mm) and vertical height H (mm). A tension-only cable is connected between two opposite corner nodes of the frame, forming a diagonal load-transfer path (red dotted line in Figure 1).

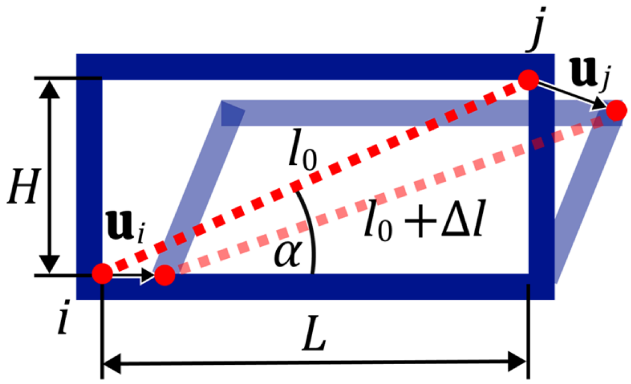


Figure 1. Simplified rectangular frame cell reinforced by a prestressed diagonal cable.

The initial undeformed cable length l_0 (mm) is determined from the frame geometry as:

$$l_0 = \sqrt{L^2 + H^2}. \tag{1}$$

The orientation of the cable with respect to the global Cartesian coordinate system is defined by the angle α (rad). The corresponding direction cosines are expressed as:

$$c = \cos\alpha = L/l_0 \qquad s = \sin\alpha = H/l_0, \tag{2}$$

where α—cable inclination angle, rad; c—horizontal direction cosine; s—vertical direction cosine.

Under external loading, the rectangular frame undergoes deformation, resulting in a displacement of the cable end node represented by the nodal displacement vector $\mathbf{u}_j$ (mm).

As a consequence, the cable experiences an elongation Δl (mm) and its length increases from the initial value l_0 to a deformed configuration $l = l_0 + \Delta l$ (mm). The geometrical parameters introduced above form the basis for the subsequent formulation of cable elongation, tension-force development and stiffness enhancement of the reinforced frame structure.

The mechanical response of the prestressed diagonal cable is governed by the relative displacement of its end nodes. Considering a cable element connecting nodes i and j,

the cable elongation Δl_{ij} (mm) can be expressed as the projection of the relative nodal displacement onto the cable axis:

$$\Delta l_{ij} = \mathbf{n}_{ij}^T(\mathbf{u}_j - \mathbf{u}_i), \tag{3}$$

where $\mathbf{u}_i$—displacement vector of node i, mm; $\mathbf{u}_j$—displacement vector of node j, mm; $\mathbf{n}_{ij}$—unit vector directed along the cable axis; T—transpose operator. Thus, $\mathbf{n}_{ij}^T$ denotes the transpose of the unit direction vector $\mathbf{n}_{ij}$. The unit direction vector is defined by the cable orientation as:

$$\mathbf{n}_{ij}^T = \begin{bmatrix} c & s \end{bmatrix}. \tag{4}$$

Equation (3) indicates that only the component of the relative nodal displacement acting along the cable axis contributes to cable elongation. Displacement components perpendicular to the cable direction do not generate axial deformation and therefore do not affect the cable force.

Once the cable elongation has been determined, the corresponding axial force can be obtained. In contrast to conventional truss elements, the diagonal cable considered in this study is assumed to carry only tensile loads and to resist no compression. This assumption reflects the actual mechanical behaviour of steel cables and corresponds to the "Tension Only" option implemented in the Ansys Mechanical environment. The axial force developed in the cable is governed by the combined effect of the initial pretension force and the additional elastic deformation induced by structural loading. Accordingly, the cable force can be expressed as:

$$T_{ij} = \begin{cases} T_0 + k_c\Delta l_{ij}, & T_0 + k_c\Delta l_{ij} > 0 \\ 0, & T_0 + k_c\Delta l_{ij} \le 0 \end{cases}, \tag{5}$$

where T_{ij}—axial force in the cable element between nodes i and j, N; T_0—initial pretension force in the cable, N; k_c—longitudinal cable stiffness, N/mm.

Equation (5) indicates that the cable develops force only when the resultant tensile action remains positive. If the relative nodal displacement causes the cable to unload to the point where the total axial force becomes zero or negative, the cable becomes inactive and no longer contributes to the structural response. For computational convenience, Equation (5) may be written in the compact form:

$$T_{ij} = max(0, T_0 + k_c\Delta l_{ij}), \tag{6}$$

which directly represents the tension-only behaviour adopted in the numerical model.

The tension-only cables contribute to the overall structural stiffness through both elastic deformation and initial pretension. The total potential energy stored in a cable-reinforced frame can therefore be expressed as the sum of the strain energy of the frame members, the energy stored in the cables and the work performed by external loads.

Accordingly, the total potential energy of the system is defined as:

$$\Pi = \frac{1}{2}\mathbf{u}^T\mathbf{K}_b\mathbf{u} + \sum_{e=1}^{m}\left[\frac{1}{2}k_{c,e}(\Delta l_e)^2 + T_{0,e}\Delta l_e\right] - \mathbf{F}^T\mathbf{u}, \tag{7}$$

where Π—total potential energy of the cable-reinforced frame system, N·mm; $\mathbf{u}$—global nodal displacement vector of the frame structure, mm; $\mathbf{K}_b$—stiffness matrix of the bare tubular frame (beam members only), assembled from the element contributions of the structural members, N/mm; m—total number of cable elements; e—cable element index; $k_{c,e}$—axial stiffness of cable element e, N/mm; Δl_e—elongation of cable element e, evaluated consistently with (3), mm; $T_{0,e}$—initial pretension force in cable element e, N; $\mathbf{F}$—global

external load vector, N. The first term represents the strain energy accumulated in the structural frame; the second term accounts for the elastic and prestress contributions of the cable system; and the last term corresponds to the work of external forces.

Application of the principle of minimum potential energy to the total potential energy functional defined in (7) yields the governing equilibrium equation of the cable-reinforced structure:

$$\mathbf{F} = \mathbf{K}_{eff}\mathbf{u}_c = (\mathbf{K}_0 + \sum_{e=1}^{m}(\mathbf{K}_{c,e} + \mathbf{K}_{g,e}))\mathbf{u}_c, \tag{8}$$

where $\mathbf{K}_{eff}$—effective global stiffness matrix of the cable-reinforced frame, N/mm; $\mathbf{K}_0 \equiv \mathbf{K}_b$—the assembled global stiffness matrix of the baseline bus body frame, retained here in the global notation used for the effective matrix $\boldsymbol{K}_{eff}$, N/mm; $\mathbf{K}_{c,e}$—elastic stiffness matrix associated with the axial deformation of cable element e, N/mm; $\mathbf{K}_{g,e}$—geometric stiffness matrix generated by the pretension force in cable element e, N/mm; $\mathbf{u}_c$—global nodal displacement vector of the cable-reinforced model, mm.

The term $\mathbf{K}_{c,e}$ represents the conventional elastic stiffness contribution resulting from cable elongation, whereas $\mathbf{K}_{g,e}$ accounts for the geometric stiffness induced by the initial pretension force.

Consequently, the proposed reinforcement concept increases the overall stiffness of the bus body through both material and geometric mechanisms. The effective stiffness matrix introduced in (8) is assembled from the contributions of individual cable elements distributed throughout the bus body structure. Therefore, the stiffness characteristics of a single prestressed cable element must first be established.

For a two-dimensional cable element connecting nodes i and j, the elastic stiffness matrix associated with axial deformation can be expressed as:

$$\mathbf{K}_{c,e} = k_{c,e}\begin{bmatrix} c^2 & cs & -c^2 & -cs \\ cs & s^2 & -cs & -s^2 \\ -c^2 & -cs & c^2 & cs \\ -cs & -s^2 & cs & s^2 \end{bmatrix}, \tag{9}$$

where $k_{c,e}$—axial cable stiffness, N/mm; c = cos α and s = sin α– direction cosines of the cable element.

In addition to the elastic contribution, the initial pretension force generates a geometric stiffness component that increases the cable's resistance to transverse deformation. The corresponding geometric stiffness matrix is given by:

$$\mathbf{K}_{g,e} = \frac{T_0}{l_0}\begin{bmatrix} s^2 & -cs & -s^2 & cs \\ -cs & c^2 & cs & -c^2 \\ -s^2 & cs & s^2 & -cs \\ cs & -c^2 & -cs & c^2 \end{bmatrix}. \tag{10}$$

The total stiffness matrix of the cable element is therefore obtained as the sum of the elastic and geometric contributions according to (9) and (10): $\mathbf{K}_e = \mathbf{K}_{c,e} + \mathbf{K}_{g,e}$. This equation demonstrates that the proposed cable reinforcement mechanism enhances the structural response through two complementary effects. The first originates from the elastic stretching of the cable, whereas the second arises from the geometric stiffening induced by the pretension force. Consequently, the prestressed cable system contributes not only to increased material stiffness but also to improved geometric stability of the bus body structure.

Since each active tensioned cable introduces an additional positive stiffness contribution, the cable-reinforced system exhibits a higher effective stiffness than the baseline frame.

Consequently, under the same external loading conditions, the displacement response of the reinforced model is expected to be lower than that of the baseline model.

The efficiency of the cable reinforcement can be evaluated using the relative reductions in displacement and stress:

$$\eta_u = \frac{u_{0,max} - u_{c,max}}{u_{0,max}} 100\%, \qquad \eta_\sigma = \frac{\|\sigma_{0,max}\| - \|\sigma_{c,max}\|}{\|\sigma_{0,max}\|} 100\%, \tag{11}$$

where η_u, η_σ—relative reduction in maximum total deformation and maximum equivalent stress respectively, %; $u_{0,max}$, $u_{c,max}$—maximum total deformation of the baseline model and the cable-reinforced model, respectively, mm; $\sigma_{0,max}$, $\sigma_{c,max}$—maximum equivalent stress in the baseline model and in the cable-reinforced model respectively, Pa.

This formulation provides a direct analytical basis for interpreting the finite-element results, where lower displacement and stress values indicate the mechanical effectiveness of the prestressed cable reinforcement. Although the numerical results reported below are expressed directly as percentage changes, Equation (11) is retained as the formal definition of these measures, so that the proposed assessment procedure remains reproducible and transferable to other body-frame configurations and loading cases.

For a rectangular bus body cell, one of the dominant deformation modes is racking, in which the frame tends to transform from a rectangular shape into a parallelogram-like configuration.

Assuming small-angle racking deformation and linear kinematics, the elongation of the active diagonal cable can be estimated from the first-order variation in the diagonal length. Since the initial cable length is defined by (1) and the horizontal displacement of the upper corner associated with small-angle racking deformation can be approximated as $\delta \approx H\gamma$, the cable elongation can be expressed as:

$$\Delta l = \left(\frac{\partial l_0}{\partial L}\right)\delta = \left(\frac{L}{l_0}\right) H\gamma = \left(\frac{L \cdot H}{l_0}\right)\gamma, \tag{12}$$

where γ—racking angle, rad. Substituting the cable elongation caused by racking deformation into the axial force relation gives the elastic contribution of the diagonal cable to the angular stiffness of the frame cell.

Equation (12) is based on the small-angle approximation $\tan\gamma = \gamma$. In the present analytical formulation, $|\gamma| \leq 10^\circ$ (approximately 0.175 rad) is adopted as a practical small-angle range, for which the difference between $\tan\gamma$ and γ remains approximately 1% or less [126]. This approximation is intended only to describe the initial racking response. In the finite-element analyses, no such angular restriction was imposed, since the structural response was calculated directly using the geometrically nonlinear formulation with Large Deflection enabled. Thus, the effective racking stiffness of the reinforced rectangular cell can be written as:

$$K_{\gamma,\mathrm{eff}} = K_{\gamma,0} + k_c \left(\frac{L \cdot H}{l_0}\right)^2 + K_{\gamma,g}, \tag{13}$$

where $K_{\gamma,\mathrm{eff}}$—effective racking stiffness of the reinforced frame cell, N·mm/rad; $K_{\gamma,0}$—initial racking stiffness of the baseline frame cell without cable reinforcement, N·mm/rad; $K_{\gamma,g}$ —geometric stiffness contribution arising from the initial cable pretension force T_0, N·mm/rad.

The term $K_{\gamma,g}$ represents the equivalent geometric contribution to the racking stiffness arising from cable pretension. It corresponds to the angular-stiffness counterpart of the geometric stiffness matrix $\mathbf{K}_{g,e}$ introduced in (10). It can be seen that the elastic cable contribution is proportional to $\left(\frac{L \cdot H}{l_0}\right)^2$, indicating that the reinforcement effect becomes

more pronounced as the dimensions of the rectangular frame cell increase. Consequently, diagonal cable reinforcement is particularly effective in structural regions characterized by large window bays, door openings, roof frames and floor-frame sections.

Equation (13) demonstrates that the increase in racking stiffness is governed by two cable-related mechanisms: elastic resistance due to cable elongation and geometric stiffness generated by pretension. Therefore, the prestressed diagonal cable system is expected to be most effective in large rectangular bus-body regions, where racking deformation is dominant, such as window bays, door openings, roof frames and floor-frame segments. This analytical prediction is consistent with the finite-element results presented in the following sections, in which the introduction of prestressed diagonal cables reduces displacement and stress levels under all investigated loading conditions.

When translating analytical modeling into FEA boundary conditions used in Ansys Mechanical (Figure 2), the following cable parameters were adopted for the numerical model: the longitudinal cable stiffness k_c = 3000 N/mm, while the initial pretension force was specified as T_0 = 6000 N, which provides sufficient initial activation of the tension-only element without excessive prestress loading.

Definition	
Material	None
Type	Longitudinal
Spring Behavior	Tension Only (Beta)
Longitudinal Stiffness	3000. N/mm
Preload	Load
Load	6000. N
Suppressed	No
Spring Length	1995.6 mm

Figure 2. Ansys's definition of the longitudinal tension-only Cable Spring joint.

These parameters were selected from the geometric relation for cable length in Equation (1), the axial force formulation in Equations (5) and (6), and the stiffness contribution of the prestressed cable system described in Equations (8)–(10). The adopted values correspond to a practical steel cable with moderate pretension (Table 1), suitable for preliminary implementation in Ansys Mechanical as a tension-only element.

Table 1. Design parameters of the prestressed cable adopted for the numerical model.

Parameter	Symbol	Value	Unit
cable diameter	d_c	8	mm
cable cross-sectional area	$A_c = \pi d_c^2/4$	50.3	mm^2
effective Young's modulus	E_c	120,000	N/mm^2
cable length	l_0	2000	mm
longitudinal stiffness	$k_c = E_c A_c / l_0$	3018	N/mm
adopted stiffness in Ansys	k_c	3000	N/mm
initial pretension force in Ansys	T_o	6000	N
initial stress	$\sigma_0 = T_o / A_c$	119.3	MPa
initial elongation	$\Delta L_c = T_o / k_c$	2.0	mm

The adopted joint parameters were derived from the equivalent axial behaviour of a representative 8 mm steel cable (Table 1). For a cable cross-sectional area of 50.3 mm^2, an effective axial modulus of 120,000 N/mm^2 and a representative length of 2000 mm,

the equivalent longitudinal stiffness is $k_c = EA/L \approx 3018$ N/mm; therefore, 3000 N/mm was adopted in Ansys. An initial pretension of 6000 N corresponds to an axial stress of approximately 119.3 MPa and an initial elongation of about 2.0 mm. Thus, the adopted stiffness and pretension represent physically consistent equivalent properties of the selected cable rather than arbitrary joint parameters. The selected pretension should therefore be regarded as a physically justified baseline value for evaluating the proposed reinforcement concept rather than as an optimized value. To evaluate the sensitivity of the structural response to this parameter and to verify that the reinforcement effect was not dependent on a single pretension value, additional D-2g-CS simulations were performed using initial pretension forces of 3000, 4500, 7500, and 9000 N, while the cable stiffness, cable layout, structural geometry, material properties, loading, and boundary conditions were kept unchanged. Together with the baseline 6000 N case, the investigated range therefore covered 0.5–1.5 times the initially adopted pretension.

The present study focuses on the structural response of the bus body frame and the influence of prestressed cables on its load-carrying behaviour, rather than on the detailed mechanical behaviour of the stranded cables themselves. For this purpose, the tension-only longitudinal joint available in Ansys Mechanical provides an appropriate idealized representation, allowing the effects of cable stiffness and pretension to be introduced directly into the full bus-frame model and efficiently varied between numerical configurations. The adopted joint stiffness was derived from the equivalent axial stiffness of the physical cable, while the prescribed pretension defines its initial tensile state. This modelling approach is therefore well-suited to the comparative analysis and numerical screening performed in this study. Detailed effects associated with stranded-cable mechanics, including strand interaction, internal contact, friction, and end-fitting compliance, are not reproduced by the adopted longitudinal-joint idealization and remain outside the scope of the present study. The static load transfer through a representative anchorage assembly is assessed separately in Section 2.2.

The reference length of the representative longitudinal tension-only spring element illustrated in Figure 2 was specified as 1995.6 mm, which is comparable to the representative cable length of approximately 2.0 m adopted in the analytical model (Table 1).

2.2. Diagonal Racking Simulation in Ansys

The object of the study was the body of a low-entry city bus model “4289” produced by JSC “Ukrautobusprom”. Its body layout features a low-floor passenger area, in accordance with UNECE Regulation No. 107 (hereinafter R107), extending over more than 60% of the cabin length, whereas the rear section is elevated by 250–400 mm and accessed via one or two steps. The resulting semi-supporting frame configuration allows the use of a conventional non-portal drive axle and provides sufficient packaging volume for the main propulsion system components.

The finite-element modeling methodology employed in the present study is based on the beam-model approach previously developed by the authors [110] for evaluating the stress–strain state of spatial vehicle body structures under the conventional structural loading modes used in vehicle frame design, namely the torsion mode (single-wheel lift) and the bending mode (all wheels supported with the dynamic load coefficient k_d). Nevertheless, the previously investigated loading cases did not include the combined diagonal suspension of two opposite wheels under dynamic loading (k_d), which represents the most severe quasi-static structural loading scenario considered in the present study. Accordingly, the Ansys boundary conditions included a “Fixed Support” constraint applied to the suspension-mounting flange of the front-right wheel (tag D in Figure 3a) and a “Displacement” constraint applied at the diagonally opposite wheel (tag E in Figure 3a).

The latter restricted displacement along the vertical Z-axis while permitting movement in the horizontal XY-plane—these constraints ensured the suspension of diagonally opposite wheels of the bus.

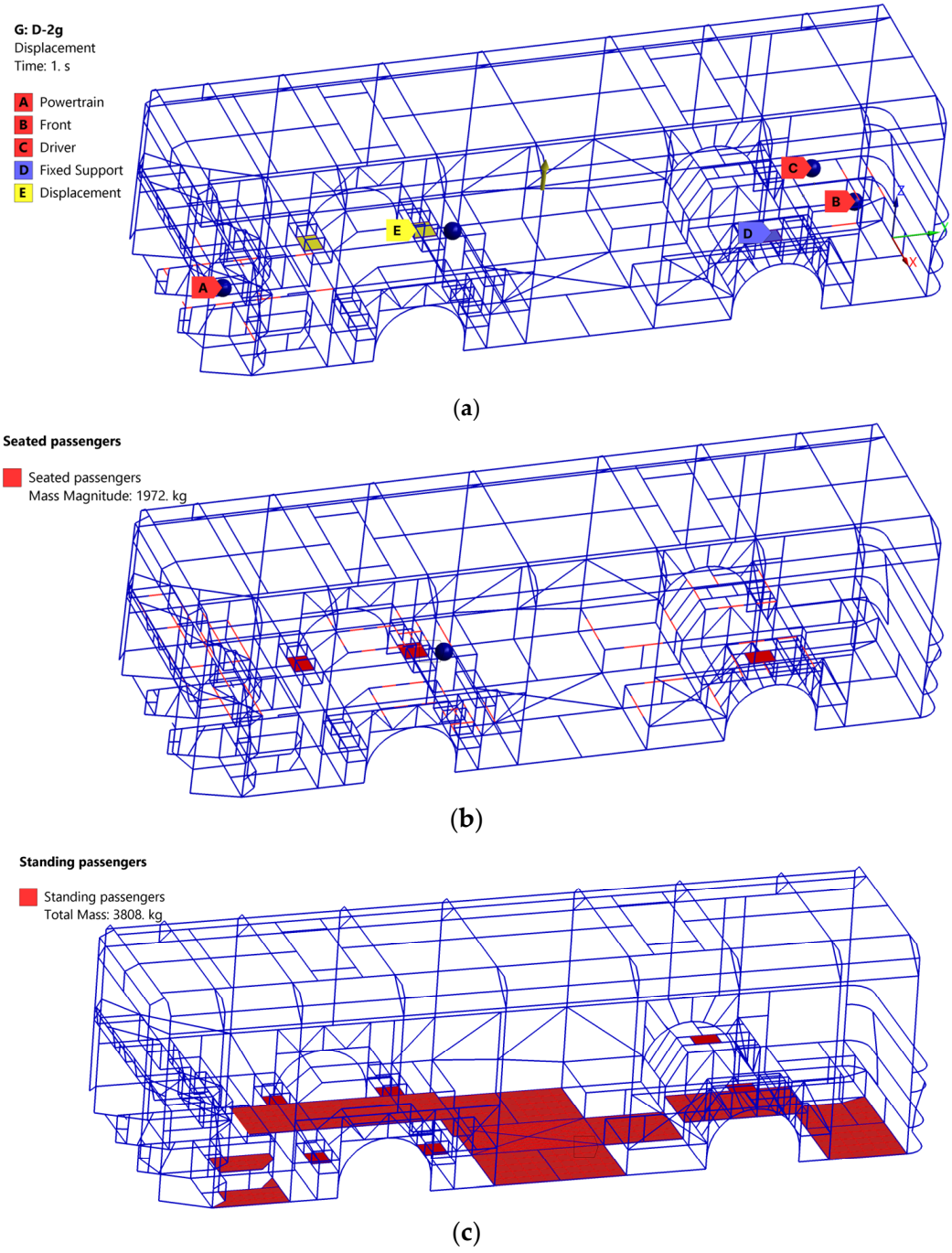


Figure 3. Boundary conditions for the loading of a bus body in Ansys: (**a**) A—powertrain, B—front assembly, C—driver, D—Fixed Support, E—Displacement. (**b**) Seated passengers. (**c**) Standing passengers.

Other boundary conditions included:

- Concentrated masses representing the principal vehicle subsystems were assigned according to the manufacturer's technical documentation: powertrain (1315 kg—tag A in Figure 3a), front assembly (220 kg—tag B in Figure 3a), driver (75 kg—tag C in Figure 3a), seated passengers (1972 kg—supports (red lines) in Figure 3b), standing passengers (3808 kg—floor elements (red areas) in Figure 3c), remaining onboard

equipment (3055 kg), together with the self-weight of the bus body (around 2400 kg); the corresponding mass allocation and mass–inertia characteristics are described in detail in the authors' previous study [95].

- The spatial tubular truss of the body frame was represented by structural members with different rectangular hollow cross-sections, including 40 × 40 × 3 mm and 80 × 40 × 3 mm members in the roof structure, 140 × 60 × 3 mm members forming the engine-compartment longitudinal beams, and 80 × 80 × 3 mm as well as 60 × 40 × 3 mm members used throughout the remaining primary and secondary load-carrying structures of the body.
- The gravitational load was introduced using the Standard Earth Gravity option (g = 9.806 m/s^2) in combination with a dynamic load coefficient of k_d = 2.0, representing the prescribed design loading condition.
- The structural members were assumed to be manufactured from S235 structural steel. The material behaviour was described by a "Bilinear Isotropic Hardening" constitutive model using properties imported directly from the Granta EduPack materials database into Ansys (Granta EduPack). The adopted material parameters were: yield strength σ_y = 252 MPa, Young's modulus $E = 2.099 \times 10^{11}$ Pa, ultimate tensile strength σ_u = 428 MPa and tangent modulus $E_t = 1.18 \times 10^9$ Pa. Geometric nonlinearity was accounted for by activating the Large Deflection option in Ansys Mechanical.

The adopted body mass of approximately 2400 kg includes the welded load-carrying structure together with the body cladding. The masses of the investigated load-carrying frames were 2312.2 kg for the conventional rectangular configuration and 1936.0 kg for the catenary-curved configuration. Nevertheless, to maintain consistency with the R100 load cases, the same total body mass of 2400 kg was used for both configurations. Thus, the lower structural mass of the catenary-curved frame was not used to reduce the applied inertial loading, thereby providing an equivalent and conservative loading basis for comparison and accounting for the fact that the masses of the cables and anchorage components were not explicitly introduced.

The cable connections between the bus body frame nodes were modelled in Ansys Mechanical 2023 R1 using the "Connection → Joints → Longitudinal—Multiple to Multiple" option with the parameters defined in Figure 2, namely the longitudinal cable stiffness k_c = 3000 N/mm and the initial pretension force T_0 = 6000 N. The "Spring Behaviour" option was set to "Tension Only", meaning that the cable carried axial tensile loads while remaining inactive under compression. This modelling strategy reproduces the physical behaviour of a prestressed steel cable with one end rigidly anchored to the structure and the opposite end tensioned and secured using a turnbuckle or an equivalent mechanical tensioning device. The adopted arrangement, comprising 29 CS joints (22 in the roof structure and 7 in the sidewalls), is illustrated in Figure 4 and represents the final outcome of an iterative numerical screening procedure. The roof cable arrangement follows the principle of criss-cross shoe lacing, thereby tying the roof structure into a unified load-carrying system. Likewise, the diagonally intersecting prestressed cables interconnect adjacent roof-frame members to increase the structure's global stiffness and promote more efficient load redistribution.

More than twenty alternative CS layouts were preliminarily investigated during an iterative numerical screening procedure. The design variables were the number of Cable Spring joints and the selection of their attachment-node pairs within the roof and sidewall frame. The mechanical parameters of the joints were kept unchanged throughout the screening, with a longitudinal stiffness of k_c = 3000 N/mm and an initial pretension of T_0 = 6000 N. The admissible design space was constrained by the existing bus-body topology: CS joints could connect only existing structural nodes, while the cable paths had

to remain compatible with the roof and sidewall frame geometry and avoid interference with functional openings and major onboard equipment. All candidate layouts were analysed using identical material properties, mesh, loading and boundary conditions, thereby isolating the influence of the number and spatial arrangement of the CS joints. The primary screening criterion was the maximum von Mises stress in the bus-body frame. Candidate configurations were iteratively generated by adding, removing or relocating CS joints, with configurations producing lower maximum stress retained for further consideration. Total deformation and the spatial distribution of highly stressed regions were monitored as secondary response indicators; however, no weighted scalar objective function was applied. To provide a transparent indication of the screening procedure without reproducing all preliminary layouts, two representative one-directional configurations were selected for explicit comparison with the retained criss-cross arrangement: D-2g-CS-1, with the CS diagonals predominantly inclined opposite to the direction of vehicle travel, and D-2g-CS-2, with the diagonals predominantly inclined in the direction of travel. Their numerical responses are reported in Section 3. This preliminary screening was intended to identify an effective configuration for demonstrating the proposed structural concept rather than to establish a formally optimized cable layout. A systematic optimization of the complete admissible design space is therefore considered a separate subject for future research.

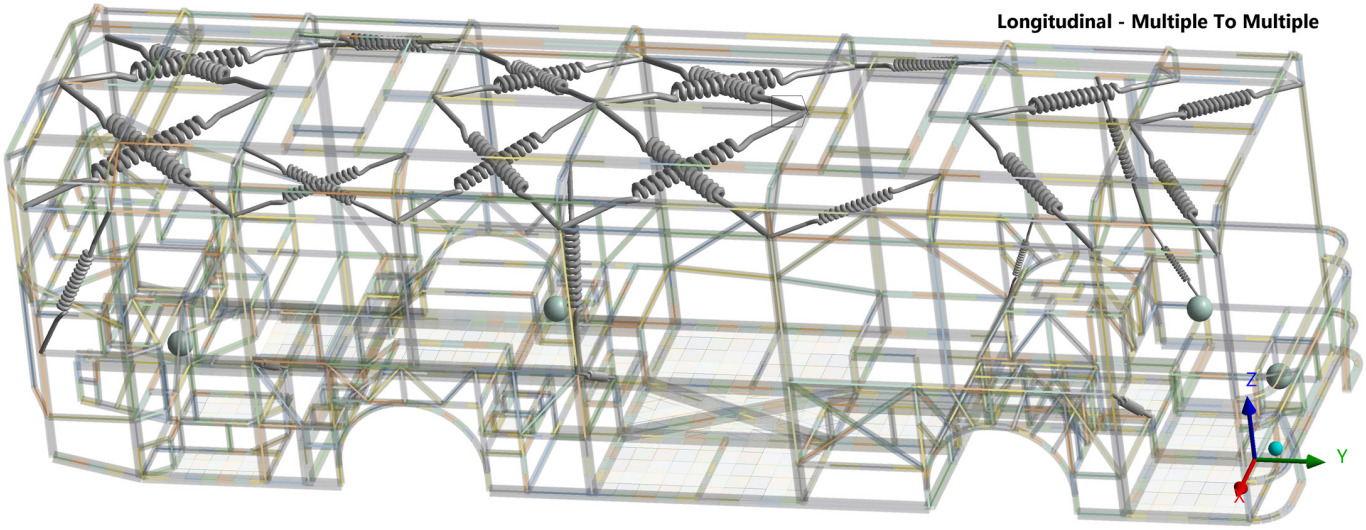


Figure 4. Implementation of the prestressed cable system in the D-2g-CS model.

To assess the structural effectiveness of integrating prestressed cable connections into the bus body frame under the most severe diagonal suspension loading condition, two finite-element models were established in Ansys: the reference model, designated D-2g (where "D" denotes the diagonal suspension loading mode and "2 g" corresponds to the dynamic load coefficient k_d = 2.0) and the cable-stiffened model D-2g-CS (Figure 4), where "CS" denotes the incorporation of Cable Spring joints.

The dynamic coefficient k_d = 2.0 was adopted in accordance with the internal structural testing methodology of the JSC "Ukrautobusprom" engineering bureau. Such internal procedures reflect empirical knowledge accumulated through previous vehicle-body design and testing experience. Within this engineering practice, dynamic coefficients in the range $k_d = 1.5 - 2.0$ are typically adopted for bus structures, while higher values are used for vehicle categories subjected to more severe dynamic loading. Accordingly, k_d = 2.0 represents the upper bound of the range conventionally adopted for bus-body structural assessment. Both diagonal orientations (D-2g and mirrored) were evaluated during the

preliminary numerical analysis. However, due to the structural asymmetry of the bus body, primarily caused by the door openings in the right sidewall, the investigated orientation resulted in higher stress and deformation levels and was therefore selected as the critical representative case. The opposite orientation resulted in lower structural response values and was not presented separately due to limitations in manuscript length.

The bus body frame was discretized in Ansys Mechanical using two-node quadratic BEAM188 elements based on Timoshenko beam theory, enabling an accurate representation of axial, bending, torsional and shear deformation behaviour of the tubular structural members, whereas the sheet-metal components of the body (floor panels) were meshed with quadrilateral SHELL181 elements. A global element size of 20 mm was adopted, resulting in a mesh comprising 47,455 finite elements (beam and shell) and 67,398 nodes, which provided a sufficiently refined representation of both the global body-frame geometry and overall structural response (Figure 5).

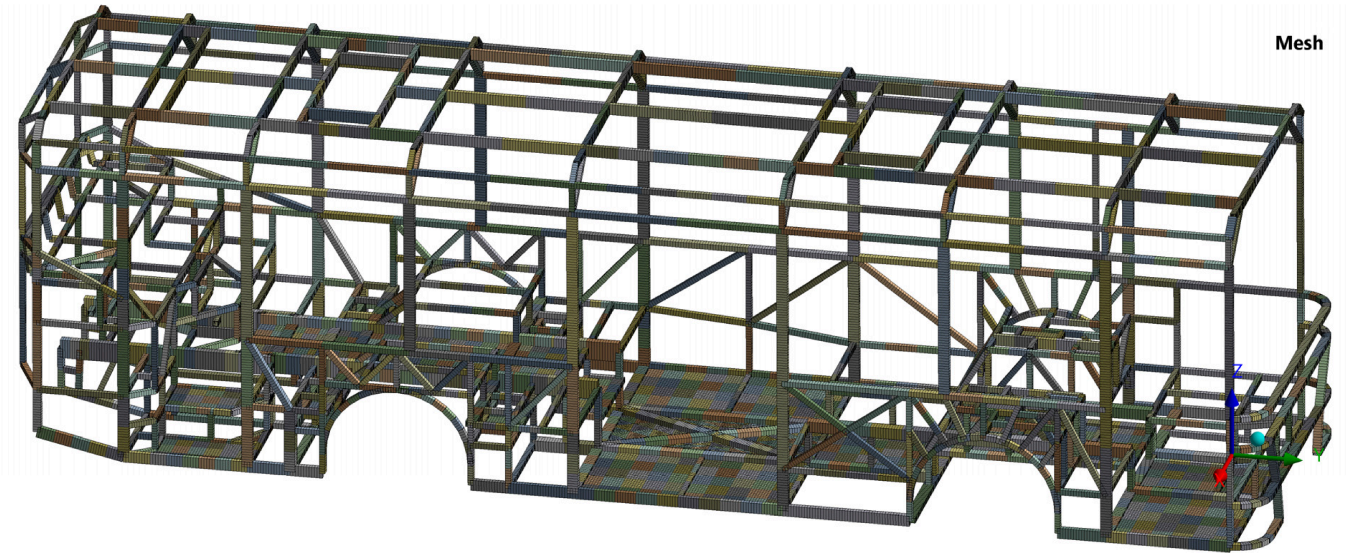


Figure 5. FEA mesh of the bus body model "4289".

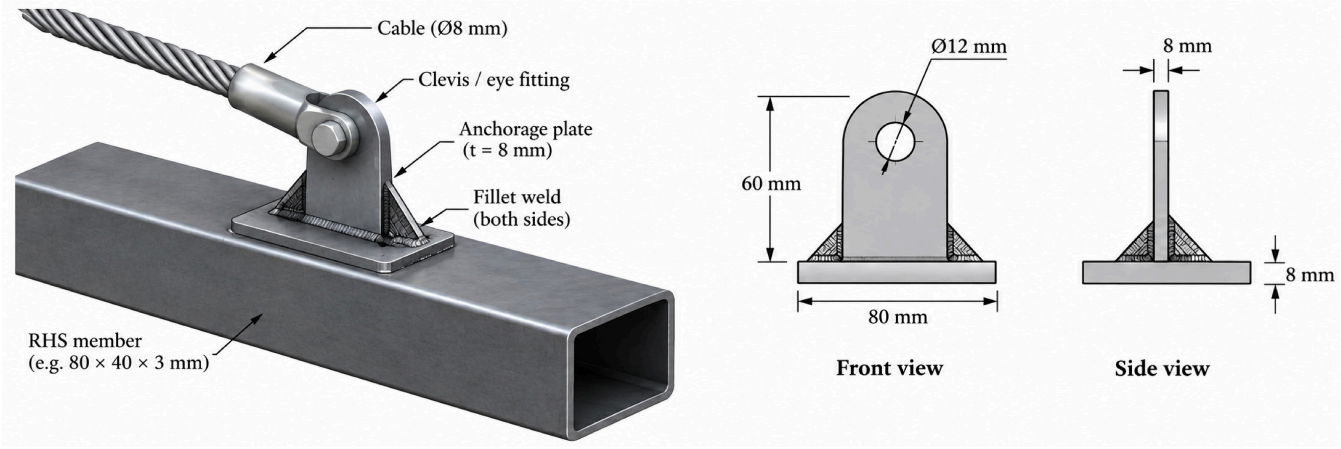
A mesh-sensitivity analysis was additionally performed using global element sizes of 50, 30, and 20 mm (Table 2). Refinement from 50 to 20 mm increased the number of finite elements from 12,751 to 47,455 and the number of nodes from 20,387 to 67,398, while the average mesh-quality parameters remained consistently high: Element Quality ranged from 0.978 to 0.982, Aspect Ratio from 1.084 to 1.180, Jacobian Ratio from 0.961 to 0.968, and Skewness from 0.046 to 0.055. Considering the predominantly quadratic BEAM188-based representation of the tubular frame and the stable mesh-quality metrics observed throughout the refinement, the 20 mm discretization was adopted for the subsequent finite-element simulations as the most refined of the investigated meshes.

Table 2. Mesh-sensitivity analysis and quality metrics for different global element sizes.

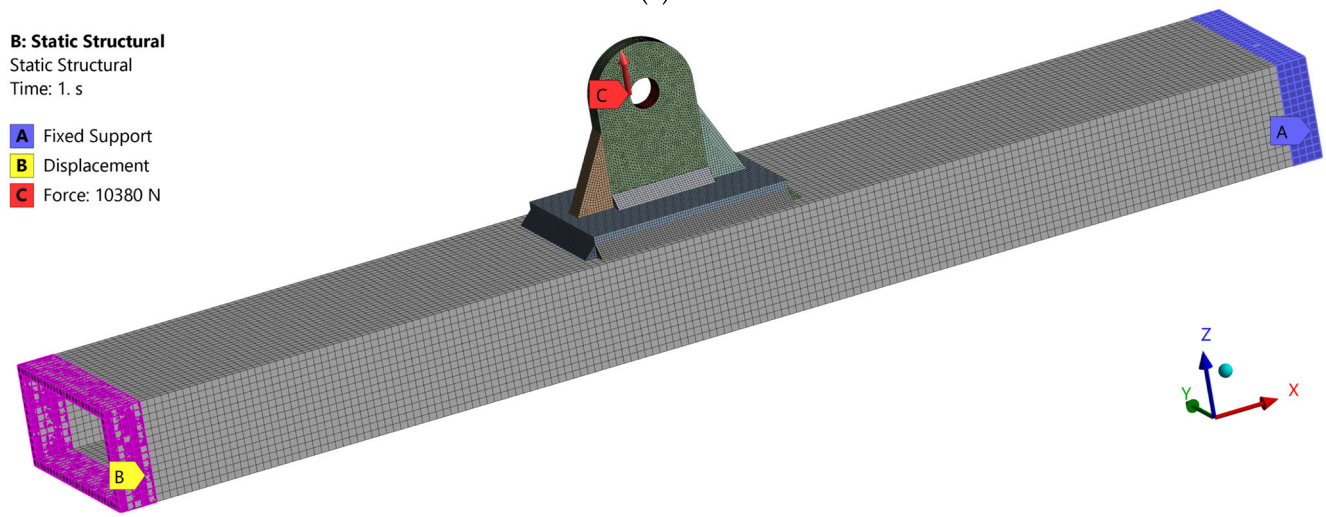
Mesh	Smoothing	Elements	Nodes	Element Quality avg.	Aspect Ratio avg.	Jacobian Ratio avg.	Skewness avg.
50 mm	Low	12,751	20,387	0.98211	1.1796	0.96117	0.05503
30 mm	Medium	26,245	39,282	0.97785	1.1170	0.96384	0.05298
20 mm	Medium	47,455	67,398	0.97800	1.0840	0.96800	0.04600

Since automatic convergence evaluation is not supported in Ansys Mechanical for results from line-body models, mesh convergence was assessed manually by comparing numerical results across different global element sizes. The relative difference was calculated as $\Delta X = (|X_{20} - X_{100}|/X_{20})\cdot 100$. For example, in an additional coarse-mesh check for the D-2g model, refining the global mesh from 100 mm to the adopted 20 mm discretization changed the maximum equivalent von Mises stress from 316.21 to 307.00 MPa, corresponding to a difference of only 3.0%.

Local anchorage assessment: since the 20 mm discretization adopted in the global bus-body model is intended to describe the overall structural response and cannot resolve the local stress gradients associated with cable-force transfer, an additional three-dimensional component-level finite-element model was developed for a representative CS anchorage. The model consisted of a 500 mm segment of an 80 × 40 × 3 mm rectangular hollow section, an 80 × 60 × 8 mm base plate, an 8 mm thick lug plate with a 12 mm diameter pin hole, two 8 mm gussets, and idealized 5 mm fillet welds connecting the anchorage assembly to the supporting member. The same S235 material representation adopted in the global body-frame analysis was used to maintain consistency between the two modelling scales (Figure 6a).



(**a**)



(**b**)

Figure 6. Representative CS anchorage used for the local component-level assessment: (**a**) anchorage geometry and principal dimensions; (**b**) finite-element mesh, boundary conditions, and applied cable force.

The component model was discretized using a nominal element size of 3 mm for the RHS (Rectangular Hollow Section) member, while the anchorage components, including the lug plate, gussets, base plate, and fillet welds, were discretized using a nominal element size of 1 mm. This finer discretization was adopted to better resolve the local stress gradients in the anchorage load-transfer region. The average element quality was 0.882, while the average aspect ratio and skewness were 1.61 and 0.172, respectively. The maximum axial cable force obtained from the baseline D-2g-CS model at T_0 = 6000 N, 10.38 kN ("Force"—tag C in Figure 6b), was applied to the cylindrical surfaces of the lug hole in the representative cable-force direction. One end of the RHS member was fully constrained ("Fixed Support"—tag A in Figure 6b), whereas at the opposite end the X- and Z-translations were restrained while the Y-direction remained free ("Displacement"—tag B in Figure 6b). This local model was introduced as a component-level static feasibility check of the anchorage load-transfer mechanism rather than as a finalized production design.

Screening-level fatigue assessment. In addition to the static structural analysis, a comparative stress-life fatigue assessment was performed for the D-2g and D-2g-CS configurations using the Fatigue Tool in Ansys Mechanical. The severe D-2g loading state was used as the maximum stress state of a constant-amplitude cycle and was therefore treated as a conservative screening envelope rather than as a representative road-load spectrum. A load ratio of $R = -0.3$ was adopted to represent partially reversed structural loading, while the Goodman relation was used for mean-stress correction. The stress-life material definition for S235J was based on the estimated fatigue data provided in the Ansys Granta EduPack Materials Data for Simulation database, which specifies a fatigue-strength range of 140–270 MPa at 10^6 cycles and 180–210 MPa at 10^7 cycles for the reference fully reversed condition $R = -1$. The imported fatigue material definition was used without further modification. Equivalent von Mises stress was selected as the fatigue stress measure, and a design life of 10^9 cycles was specified. Since the same material data, loading ratio, mean-stress correction, and fatigue settings were applied to both configurations, the resulting fatigue life and safety-factor values were used primarily for a relative comparison of the influence of CS reinforcement.

2.3. R100 Simulation in Ansys

According to UNECE Regulation No. 100 (R100), the structural integrity of battery mounting systems shall be verified under prescribed inertial loading conditions corresponding to longitudinal and transverse accelerations of 6.6 g and 5.0 g, respectively. The boundary conditions adopted for the numerical model were described in detail in the authors' previous study [111], thereby ensuring methodological continuity in the investigation of bus structural safety. The principal loading parameters applied in the Ansys model comprised the masses of the air-conditioning unit and batteries subjected to the prescribed acceleration fields, together with the corresponding concentrated loads applied at each mounting point (Table 3).

Table 3. Boundary loading conditions under the R100 longitudinal 6.6 g and transverse 5.0 g cases.

Mode	Direction	Element	m_i, kg	Points	k_d	ΣF, N	F_i, N	Axis
6.6 g	longitudinal	air-conditioning	300	9	6.6	19,423.8	2158.2	*Y*
		batteries	1875	9	6.6	121,398.8	13,488.8	*Y*
5.0 g	transverse	air-conditioning	300	9	5	14,715.0	1635.0	*X*
		batteries	1875	9	5	91,968.75	10,218.8	*x*

The remaining boundary conditions included:

- "Fixed Support" applied to the mounting flanges of the front suspension air cylinders (tag A in Figure 7);
- "Displacement" constraint allowing translational movement only along the longitudinal (Y) axis of the bus, thereby enabling realistic transverse bending and torsional deformation of the body structure under lateral loading (tag B in Figure 7);
- Standard Earth Gravity with a gravitational acceleration of g = 9.8066 m/s^2;
- Lumped masses representing the roof-mounted air-conditioning unit (tag C in Figure 7) and the battery assembly (tag D in Figure 7);
- Other concentrated masses representing the principal vehicle subsystems are inherited from the D-2g model.

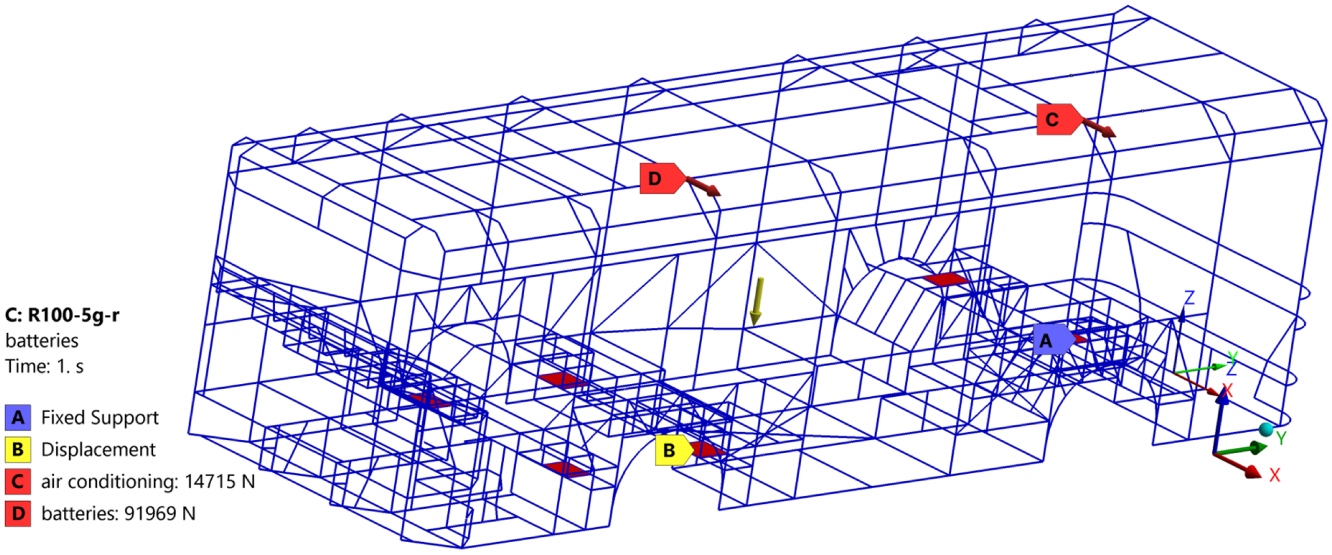


Figure 7. Boundary conditions for the UNECE R100 lateral 5 g loading case (R100-5g-r model).

For clarity, the designations of the investigated loading modes were formed according to a unified notation, in which each component identifies the regulatory basis, acceleration level and structural configuration of the bus body frame:

- R100—loading conditions according to R100;
- 6.6 g—longitudinal inertial acceleration applied to the body-frame masses;
- 5 g—transverse inertial acceleration applied to the body-frame masses;
- r—conventional rectangular body-frame cross-section;
- c—catenary-curved body-frame cross-section proposed in [92];
- CS—incorporation of Cable Spring (CS) joints into the body frame.

For example, "R100-6.6g-c" (Figure 8a) represents the finite-element model corresponding to the UNECE R100 loading condition with a longitudinal inertial acceleration of 6.6 g, a catenary-curved body-frame cross-section (c), while "R100-6.6g-c-CS" is the same model but equipped with integrated CS (Figure 8b). For simplicity, the terms "*mode*" and "*model*" are treated as equivalent throughout this paper, since each mode corresponds to a unique combination of structural configuration and loading condition.

Since the battery system considered in the present model is roof-mounted, the inter-window pillars play a key structural role in transferring the prescribed inertial loads from the roof assembly to the bus body's lower load-bearing frame. Consequently, their stiffness has a major influence on the transmission and redistribution of the prescribed longitudinal (6.6 g) and transverse (5 g) inertial loads throughout the body structure. To evaluate the influence of Cable Spring joints installed exclusively within the inter-window pillars on

the overall structural stiffness of the bus body, without interference from additional roof reinforcement (as in the D-2g-CS model), 18 CS were incorporated only into the inter-window pillars of the R100-6.6g-c-CS and R100-5g-c-CS models (Figure 8b). The roof structure itself remained identical to that of the reference catenary-curved body-frame models (R100-6.6g-c and R100-5g-c), i.e., without any CS integration.

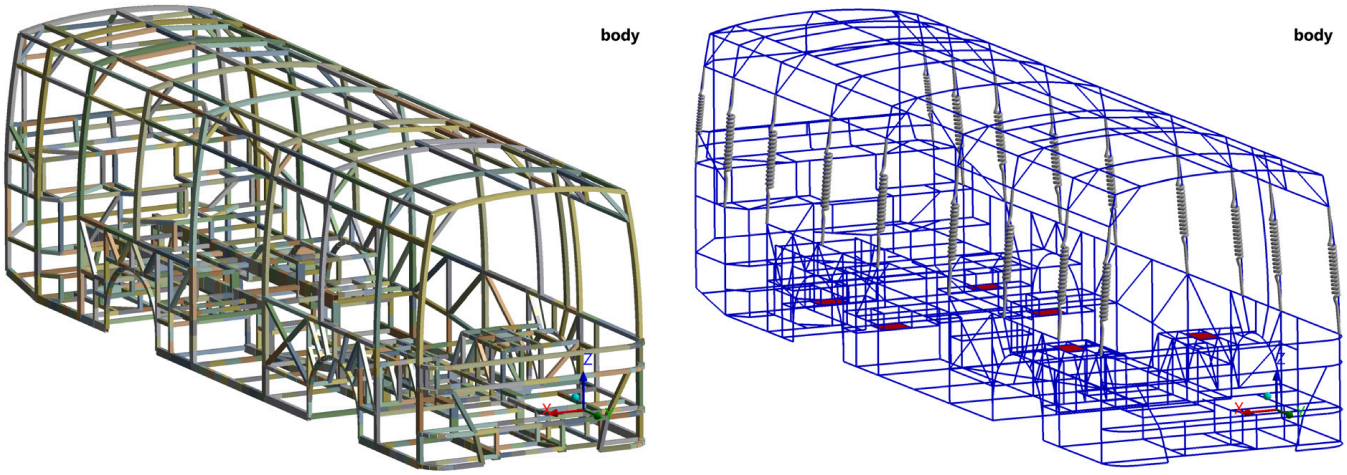


Figure 8. Catenary-curved body-frame Ansys model: (**a**) R100-6.6g-c/R100-5g-c. (**b**) R100-6.6g-c-CS/R100-5g-c-CS with integrated Cable Spring joints.

The different numbers and locations of CS joints used in the investigated models were intentionally selected to match the structural function being evaluated. The D-2g-CS model includes 29 CS joints distributed between the roof and sidewalls to assess their contribution to global racking stiffness. In contrast, the R100 models include only 18 CS joints located in the inter-window pillars. This differentiation allows the contribution of the bow–bowstring reinforcement of the pillars to be evaluated without superimposing the effect of additional roof cables.

3. Results

The effectiveness of the proposed prestressed Cable Spring (CS) reinforcement strategy was assessed through a comparative finite-element analysis of the investigated bus body configurations under diagonal racking and UNECE R100 inertial loading conditions. The structural response was evaluated using the von Mises equivalent stress distribution, safety-factor maps, and maximum total deformation, thereby quantifying the influence of the catenary-curved geometry and integrated CS joints on the global stiffness and load redistribution of the body frame. Strain was not considered as a separate comparative parameter in the present study. For the adopted S235 constitutive model, the strain response is inherently included in the stress–strain relationship used by the finite-element formulation. At the same time, the primary engineering criteria of interest were the equivalent stress relative to the material yield strength and the global displacement response of the bus body. Therefore, equivalent stress, safety factor, and total deformation were selected as the principal parameters for comparing the investigated structural configurations.

3.1. Bus Body Diagonal Racking

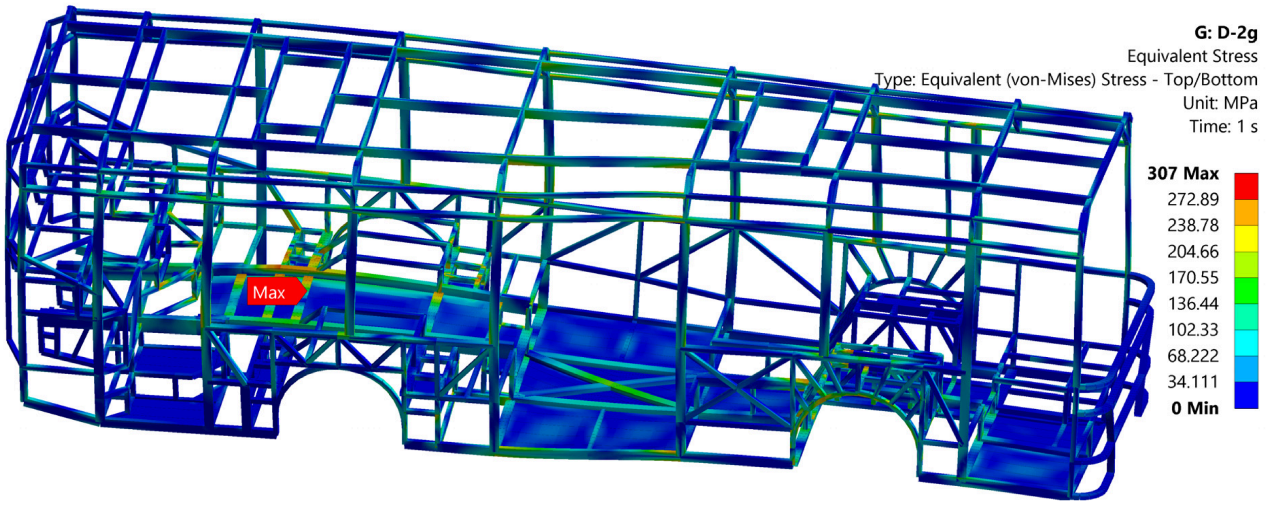
The structural strength of the bus body was evaluated using the von Mises equivalent stress criterion, which is widely accepted for isotropic ductile materials such as structural

steels. According to the von Mises yield criterion, yielding occurs when the equivalent stress satisfies:

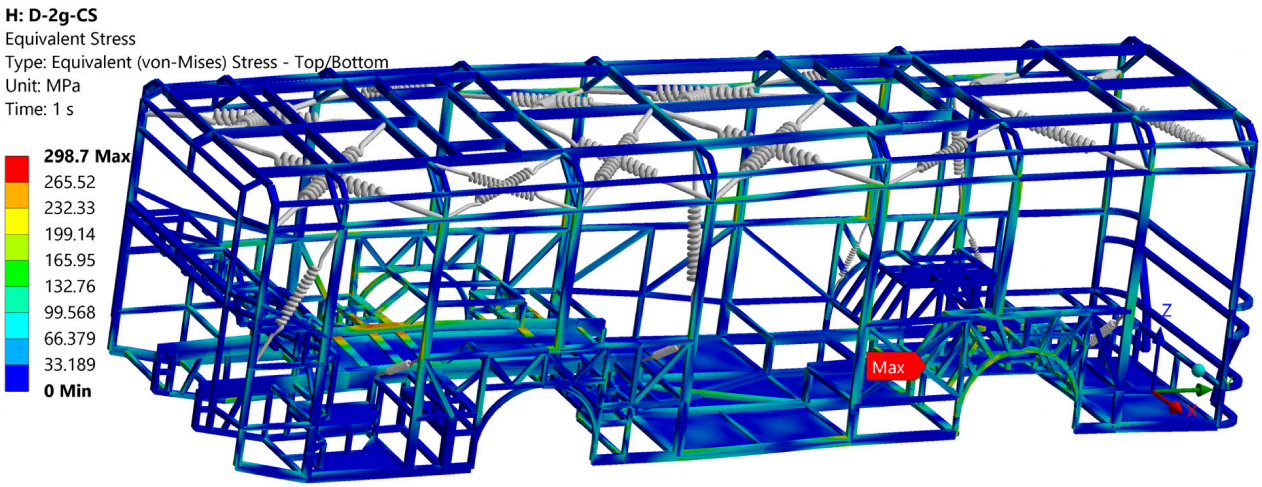
$$\sigma_{vM} = \sqrt{\left((\sigma_1 - \sigma_2)^2 + (\sigma_2 - \sigma_3)^2 + (\sigma_3 - \sigma_1)^2\right)/2} \geq \sigma_y, \sigma_y = SF \cdot \sigma_{vM}, \quad (14)$$

where σ_1, σ_2 and σ_3—principal stresses, MPa; SF—corresponding safety factor used in Ansys is determined relative to the yield strength σ_y. $SF > 1$ indicates an elastic strength reserve, $SF = 1$ corresponds to the onset of yielding, and $SF < 1$ indicates that the von Mises equivalent stress exceeds the yield strength. The safety-factor values reported below were obtained directly from the Ansys Safety Factor results using the material properties defined in Engineering Data; minor differences from values calculated using the rounded material parameters reported in the text may therefore occur.

Following the integration of CS joints, the maximum von Mises stress decreased by 2.7% (from 307.00 to 298.70 MPa—Table 4) while its location shifted from the suspension-mounting cross-members in the rear overhang (D-2g mode in Figure 9a) to the front-right wheel-arch truss (D-2g-CS mode in Figure 9b). This redistribution is favourable because it reduces the stress concentration in the vicinity of the engine compartment and may limit the relative displacement of the powertrain components.



(**a**)



(**b**)

Figure 9. Equivalent stress (von Mises) maps under diagonal racking: (**a**) D-2g. (**b**) D-2g-CS.

Table 4. Comparison of structural response parameters under diagonal racking.

Mode	T_0, N	$\sigma_{vM,max}$, MPa	$\sigma_{vM,ave}$, MPa	SF_{min}	SF_{ave}	u_{max}, mm
D-2g	-	307.00	46.18	0.83	8.86	128.39
D-2g-CS	6000	298.70	38.68	0.85	9.77	91.94
D-2g-CS	3000	296.30	38.66	0.86	9.78	93.11
D-2g-CS	4500	297.66	38.62	0.85	9.78	92.41
D-2g-CS	7500	282.62	38.84	0.90	9.74	91.58
D-2g-CS	9000	299.30	39.05	0.85	9.71	91.23

The pretension sensitivity analysis demonstrated that the global structural response of the CS-reinforced body remained relatively stable over the investigated range of T_0 = 3000–9000 N. The maximum total deformation decreased monotonically from 93.11 mm at 3000 N to 91.23 mm at 9000 N, corresponding to a variation of only 2.0% across the entire pretension range. Relative to the D-2g reference model without CS reinforcement (u_{max} = 128.39 mm), all investigated pretension levels provided a substantial reduction in maximum deformation, ranging from 27.5% to 28.9%. Similarly, the average von Mises stress remained within a narrow range of 38.62–39.05 MPa, corresponding to reductions of 15.4–16.4% relative to the reference value of 46.18 MPa, while the average safety factor varied only between 9.71 and 9.78. In contrast, the maximum von Mises stress exhibited a non-monotonic response, ranging from 282.62 to 299.30 MPa and reaching its lowest value at T_0 = 7500 N. However, the lower peak stress obtained at 7500 N should not be considered in isolation when selecting the pretension level. Increasing T_0 from 6000 to 7500 N raises the initial cable stress from approximately 119.3 to 149.1 MPa and correspondingly increases the preload transmitted to the cable anchorages, while reducing the maximum total deformation by only about 0.4% and producing virtually no improvement in the average stress response. Therefore, the adopted 6000 N pretension represents a more balanced baseline value, providing nearly the same global stiffness benefit while maintaining lower initial cable and anchorage loading and, consequently, a larger theoretical reserve for cyclic force fluctuations, installation tolerances, and long-term service effects. The sensitivity analysis thus confirms that the effectiveness of the CS concept is robust over a broad pretension range, while supporting 6000 N as a conservative and physically justified design value for the present comparative study.

Unless otherwise stated, the following results refer to the comparison between the baseline D-2g and D-2g-CS configurations at the adopted pretension of T_0 = 6000 N. The average stress $\sigma_{vM,ave}$ throughout the bus body decreased by a substantial 16.2% (from 46.18 to 38.68 MPa), indicating the potential for further optimization of the structural material utilization. Specifically, the reduced stress level may enable the use of smaller steel tube cross-sections, thereby reducing both material consumption and overall body weight. This observation motivates one of the future directions of the present research.

The integration of CS joints resulted in a slight increase in the minimum safety factor SF_{min} from 0.83 to 0.85 (Figure 10), while the average SF_{ave} increased more noticeably from 8.86 to 9.77 (10.3%). These results (Table 4) indicate an overall improvement in the structural safety margin of the bus body owing to the more uniform redistribution of stresses.

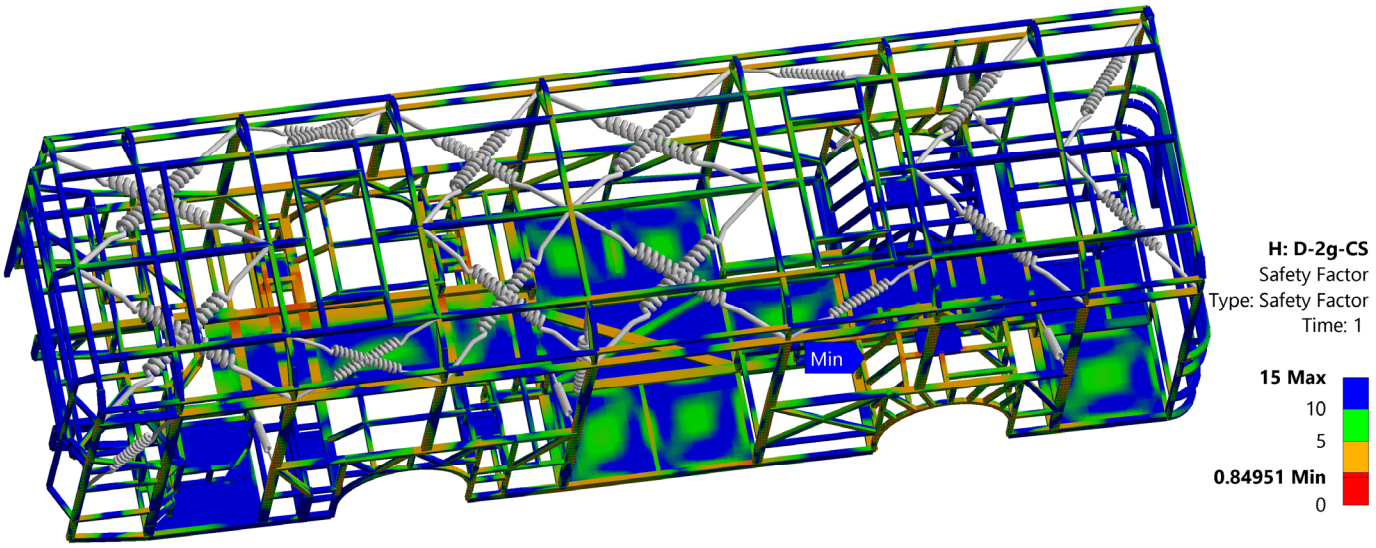


Figure 10. Safety factor map in D-2g-CS mode.

In Ansys, the "Total Deformation" $u_{\max}$ result represents the magnitude of nodal displacement relative to the initial (undeformed) configuration rather than material deformation (strain). It is calculated as the magnitude of the displacement vector:

$$u_{\max} = \sqrt{u_x^2 + u_y^2 + u_z^2}, \tag{15}$$

where u_x, u_y and u_z—displacement components along the global coordinate axes.

The integration of CS joints into the bus body structure reduced the maximum total deformation from 128.39 to 91.94 mm (−28.4%), indicating substantially improved global dimensional stability under diagonal racking. In both configurations, the location of $u_{\max}$ remained unchanged (Figure 11) and was situated at the upper right corner of the roof in the rear overhang.

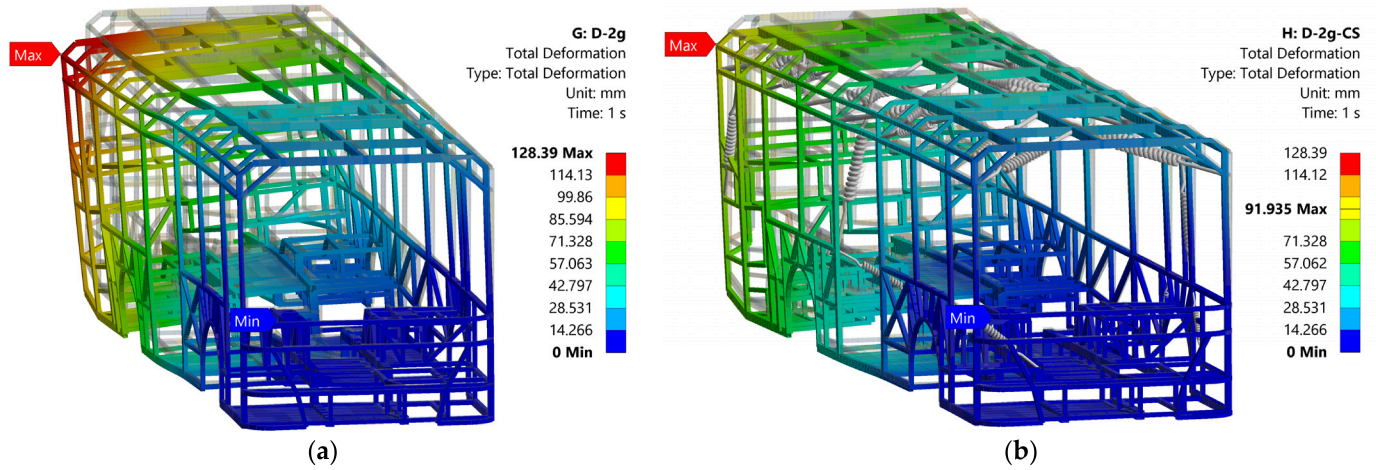


Figure 11. Deformation maps under diagonal racking: (**a**) D-2g. (**b**) D-2g-CS.

A screening-level serviceability assessment was additionally performed at the powertrain mounting point located nearest to the region of maximum global deformation. The allowable displacement specified by the powertrain manufacturer is 50 mm. In the reference D-2g model, the total displacement at this point reached 73.61 mm, corresponding to a utilization ratio of 1.47 and an exceedance of 47.2%. After introducing the CS reinforcement, the displacement decreased to 54.77 mm, corresponding to a utilization ratio

of 1.10 and an exceedance of 9.5%. Thus, the CS system reduced the displacement at this functionally critical point by 25.6%, while the absolute exceedance of the allowable limit decreased from 23.61 to 4.77 mm, i.e., by approximately 79.8%. Although the reinforced configuration still slightly exceeds the specified serviceability limit, the result provides a bounded quantitative indication of substantially improved local dimensional stability under diagonal racking.

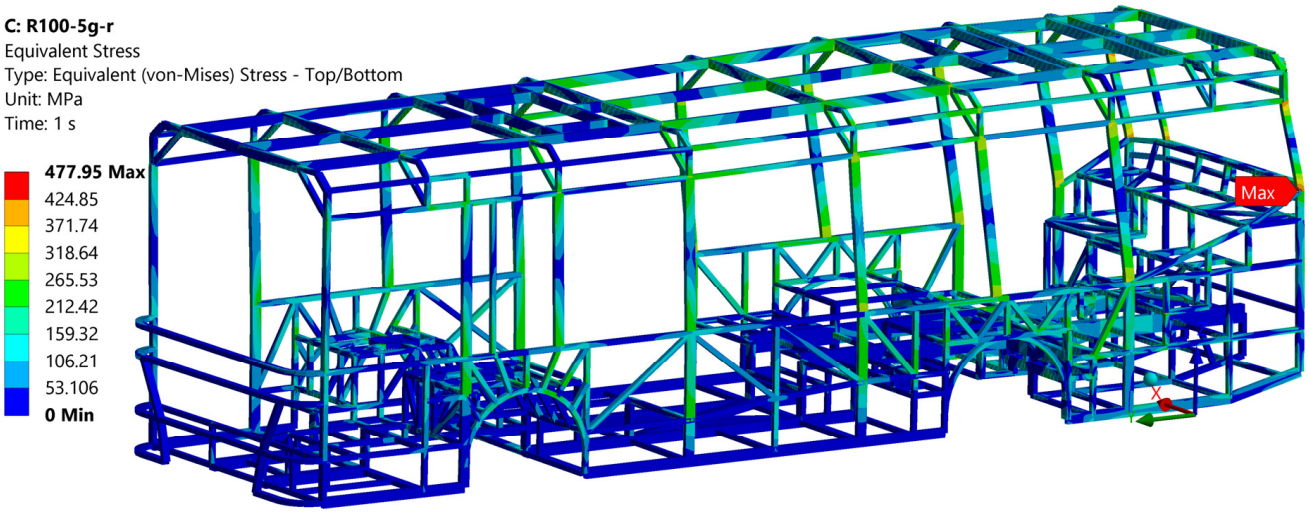
The screening-level fatigue analysis further indicated a beneficial effect of the CS reinforcement under the adopted constant-amplitude loading assumption. For the reference D-2g configuration, the minimum predicted fatigue life was 59,465 cycles, whereas the D-2g-CS model reached 110,810 cycles, corresponding to an increase of approximately 86.3% (1.86 times). The minimum fatigue safety factor increased from 0.714 to 0.734, i.e., by approximately 2.8%. The critical fatigue locations were not identical in the two configurations, indicating that the introduction of CS joints modifies not only the magnitude but also the spatial distribution of fatigue-critical stresses. Both minimum safety factors remained below unity for the specified design life of 10^9 cycles. However, these absolute values should not be interpreted as predictions of the operational service life of the bus, because the full severe D-2g loading state was repeatedly applied as a constant-amplitude cycle. Rather, the calculation provides a conservative comparative screening showing that, under identical fatigue assumptions, the CS-reinforced configuration exhibits a substantially higher minimum predicted fatigue life than the reference body frame.

3.2. Bus Body R100 Loading

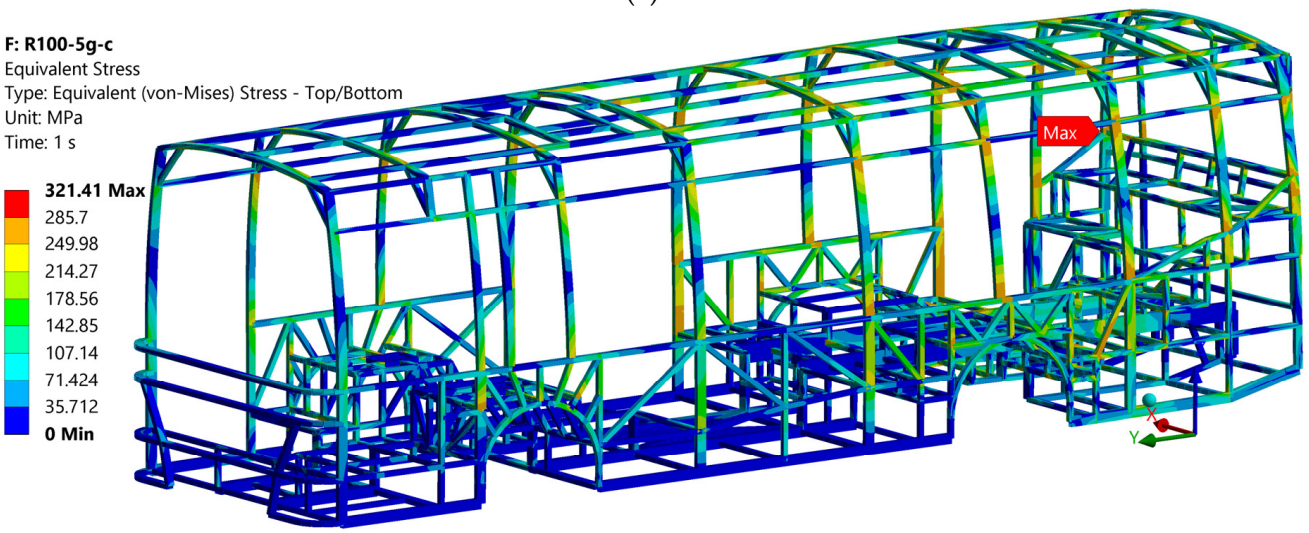
Under the R100 transverse 5 g inertial loading condition, the maximum von Mises stress $\sigma_{vM,max}$ decreased progressively from 477.95 MPa (R100-5g-r mode in Figure 12a) to 321.41 MPa (R100-5g-c mode in Figure 12b), corresponding to a 32.7% decrease resulting from the adoption of the catenary-curved cross-section. Following the additional integration of CS joints into the inter-window pillars, the maximum von Mises stress $\sigma_{vM,max}$ further decreased to 281.23 MPa (R100-5g-c-CS in Figure 12c), representing an additional 12.5% reduction and an overall decrease of 41.2% relative to the reference configuration (Table 5).

The location of the maximum von Mises stress $\sigma_{vM,max}$ (tag "Max" in Figure 12) changed considerably between the analyzed configurations. In model R100-5g-r, the maximum stress was located in the leftmost inter-window pillar of the rear overhang, whereas in R100-5g-c, it shifted to the corresponding pillar on the opposite side. Following the integration of CS joints into the inter-window pillars (R100-5g-c-CS), the global maximum stress shifted to the rear-seat support frame and reached 281.23 MPa (tag "Max" in Figure 12c), whereas the maximum von Mises stress within the inter-window pillars (sidewalls) was limited to 227.42 MPa, remaining below the yield strength (σ_y = 252 MPa) of S235 steel. Consequently, R100-5g-c-CS mode is theoretically capable of maintaining the inter-window pillars predominantly within the elastic range (Hooke's law), thereby preventing plastic deformation and better preserving the sidewall structural geometry under the investigated loading conditions.

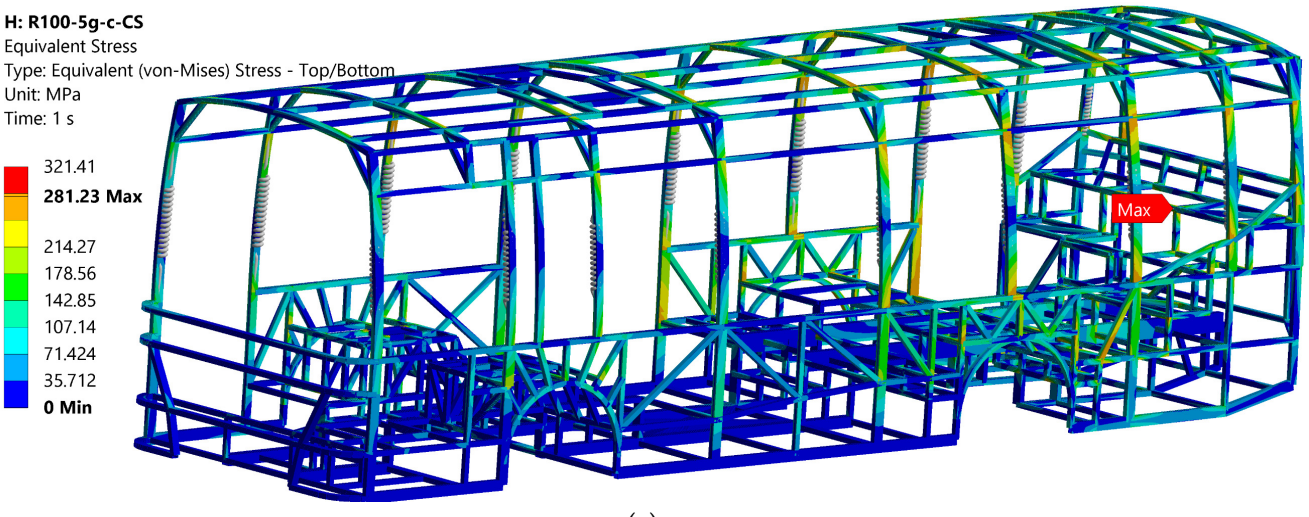
The average von Mises stress $\sigma_{vM,ave}$ decreased progressively from 72.81 MPa in the reference rectangular mode (R100-5g-r) to 67.54 MPa (−7.2%) after adopting the catenary-curved cross-section (R100-5g-c) and further to 54.86 MPa (−18.8%) following the integration of CS joints (R100-5g-c-CS), corresponding to an overall reduction of 24.7% relative to the reference configuration.



(**a**)



(**b**)

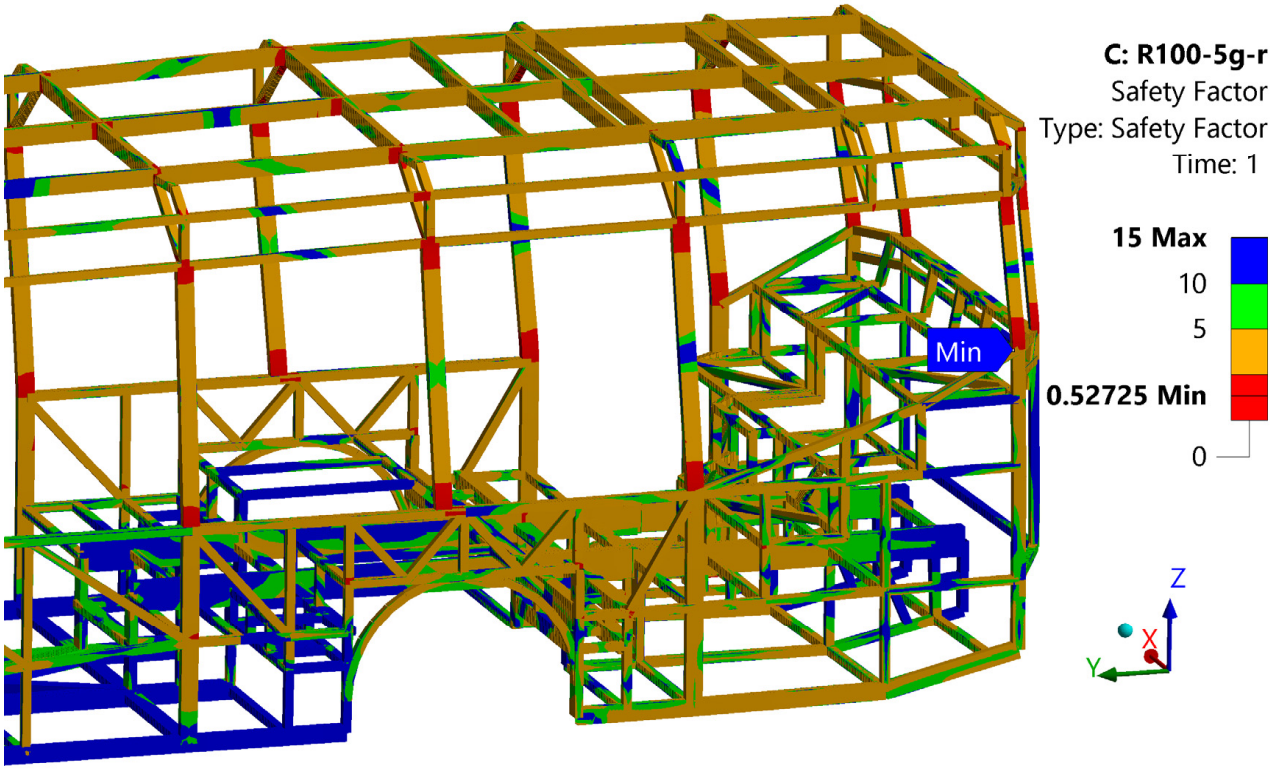


(**c**)

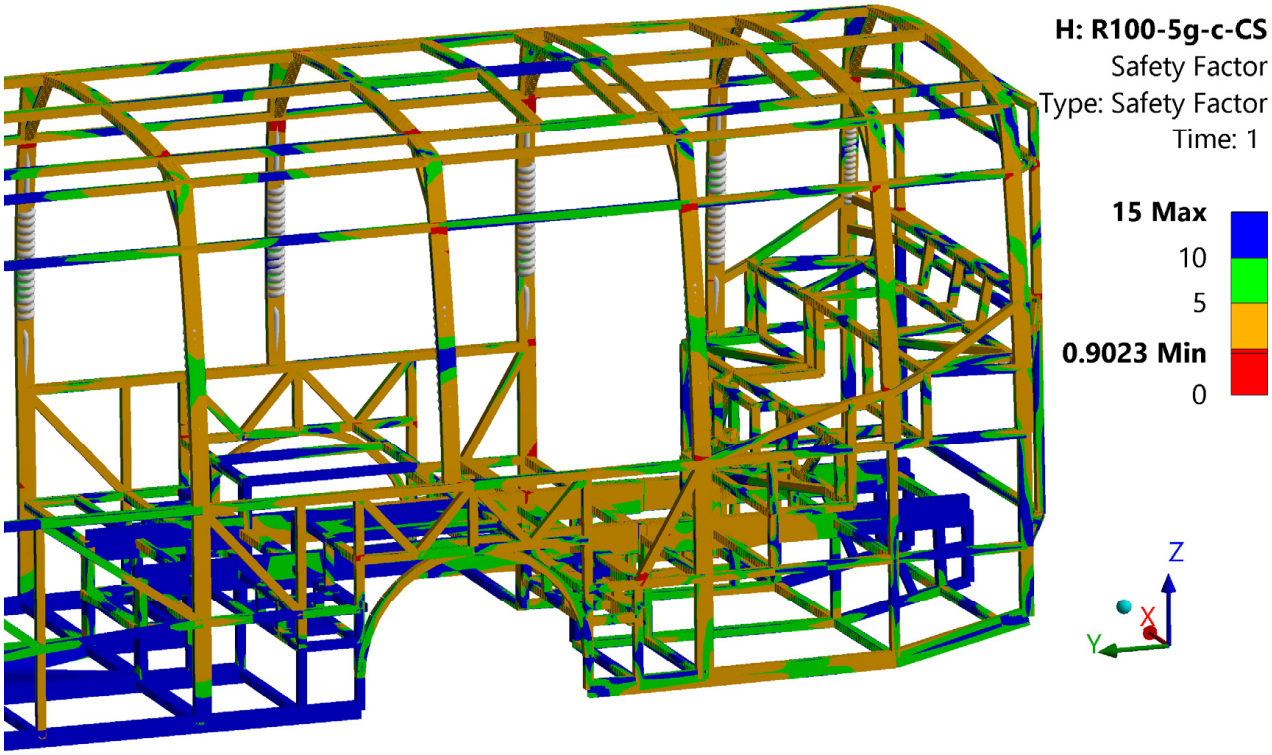
Figure 12. Equivalent stress (von Mises) maps under R100 transverse (5 g) loads: (**a**) R100-5g-r. (**b**) R100-5g-c. (**c**) R100-5g-c-CS.

The minimum safety factor SF_{min} increased from 0.53 (Figure 13a) in the reference model to 0.79 after adopting the catenary-curved cross-section (49.1%), followed by a further increase to 0.90 (Figure 13b) after integrating CS joints (13.9%), corresponding to an

overall improvement of 69.8%. The average safety factor increased from 6.87 to 7.19 (4.7%) owing to the catenary-curved cross-section and further to 8.17 (13.6%) after the integration of CS joints, representing an overall increase of 18.9% relative to the reference model.



(**a**)



(**b**)

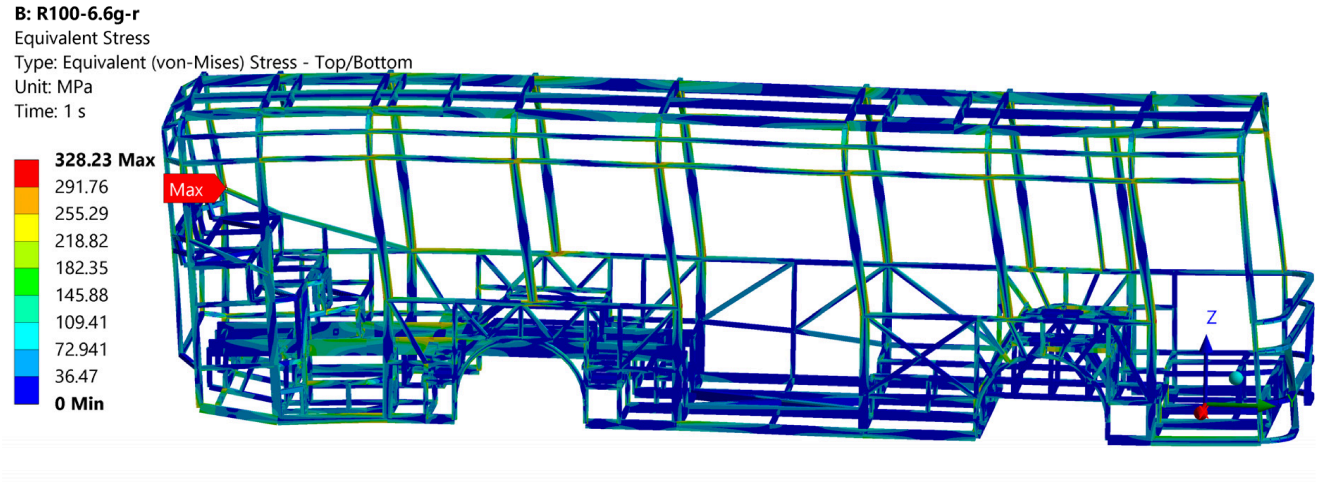
Figure 13. Safety factor maps under R100 transverse (5 g) loads: (**a**) R100-5g-r. (**b**) R100-5g-c-CS.

Table 5. Comparison of the stressed-deformed-state results under the R100 load.

Mode	$\sigma_{vM,max}$, MPa	$\sigma_{vM,ave}$, MPa	SF_{min}	SF_{ave}	u_{max}, mm
R100-5g-r	477.95	72.81	0.53	6.87	358.55
R100-5g-c	321.41	67.54	0.79	7.19	138.74
R100-5g-c-CS	281.23	54.86	0.90	8.17	89.31
R100-6.6g-r	328.23	61.95	0.77	7.59	127.88
R100-6.6g-c	309.48	61.37	0.82	7.76	109.47
R100-6.6g-c-CS	298.30	52.60	0.85	8.62	79.06

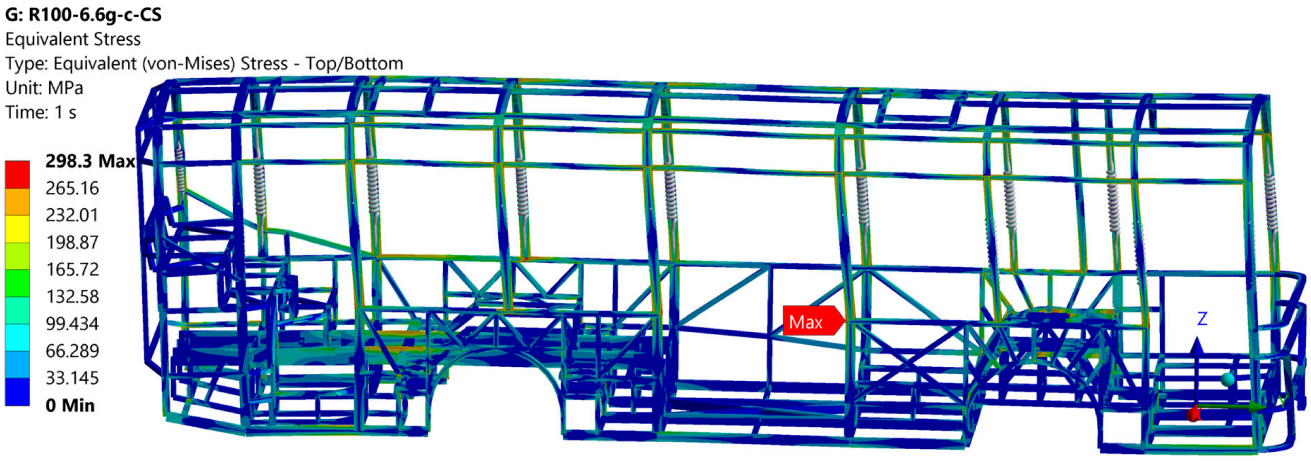
Beyond the numerical comparison, particular attention should be paid to the distribution of the safety factor within the inter-window pillars. In the reference R100-5g-r model, pronounced red regions ($SF < 1$) are observed near the upper and lower joints of the pillars (Figure 13a), indicating local yielding and the potential initiation of plastic-hinge mechanisms. Such plastic hinges are characteristic failure locations in lateral impact and rollover loading of bus body structures (e.g., UNECE R66), as they indicate the loss of elastic load-carrying capacity and may initiate permanent distortion of the body-frame geometry. In contrast, the R100-5g-c-CS model exhibits a substantially more favourable stress state. In the most highly loaded rear body section (Figure 13b), the inter-window pillars are almost entirely free of regions with $SF < 1$, suggesting that the pillars remain predominantly within the elastic range and are therefore capable of preserving the structural integrity and overall body geometry under the investigated loading condition.

The structural improvement provided by the combined catenary-curved and CS configuration was less pronounced under longitudinal 6.6 g loading than under transverse 5 g loading. Specifically, the maximum equivalent (von Mises) stress, $\sigma_{vM,max}$, decreased from 328.23 MPa in the R100-6.6g-r mode (Figure 14a) to 298.30 MPa in the R100-6.6g-c-CS (Figure 14b), corresponding to a reduction of 9.1%. Relative to the catenary-curved model alone, the addition of CS joints reduced the maximum and average von Mises stresses by 3.6% and 14.3%, respectively, and the maximum deformation by 27.8%. The structural configuration of the inter-window pillars can explain the difference between 6.6 g and 5 g results.



(**a**)

Figure 14. *Cont.*



(**b**)

Figure 14. Equivalent stress (von Mises) maps under R100 longitudinal (6.6 g) loads: (**a**) R100-6.6g-r. (**b**) R100-6.6g-c-CS.

In the transverse bus direction, each pillar has a catenary-curved profile whose ends are connected by a prestressed CS, forming a structural system analogous to an archery bow, where the curved pillar acts as the bow limb and the prestressed cable represents the bowstring. Consequently, the catenary arch and the tensioned cable jointly resist the transverse (5 g) inertial loads acting in the plane of the curved pillar, resulting in a more efficient redistribution of stresses. Under the longitudinal (6.6 g) loading condition, however, the principal inertial forces act predominantly outside this structural plane, thereby reducing the contribution of the bow–bowstring mechanism and the effectiveness of the CS joints. This directional dependence confirms that the effectiveness of the bow–bowstring mechanism is governed by the orientation of the dominant load path relative to the plane of the catenary-curved pillar and prestressed cable.

Under the longitudinal 6.6 g load, the average von Mises stress, $\sigma_{vM,ave}$, decreased from 61.95 MPa in the reference model to 61.37 MPa after adopting the catenary-curved cross-section (0.9%), followed by a further reduction to 52.60 MPa after integrating CS joints (14.3%), corresponding to an overall decrease of 15.1% (Table 5). The minimum safety factor SF_{min} increased from 0.77 to 0.82 (6.5%) and further to 0.85 (3.7%), while the average safety factor SF_{ave} increased from 7.59 to 7.76 (2.2%) and subsequently to 8.62 (11.1%), representing an overall improvement of 13.6% relative to the reference model.

Among the evaluated parameters, maximum total deformation u_{max} is of particular importance because, unlike averaged stress $\sigma_{vM,ave}$ and safety-factor SF_{min} values, it directly characterizes the global distortion of the body frame. The greatest structural improvement was achieved under the R100 transverse (5 g) loading condition, where u_{max} decreased from 358.55 mm (Figure 15a) in the reference rectangular model to 138.74 mm after adopting the catenary-curved cross-section (61.3%) and further to 89.31 mm following the integration of CS joints (Figure 15b), corresponding to an overall reduction of 75.1%.

The deformation maps (Figure 15 a,b) reveal a pronounced non-uniform stiffness distribution in the reference rectangular body frame (R100-5g-r), with the largest deformation concentrated in the rear body section, where u_{max} was recorded (tag "max"). Under the longitudinal (6.6 g) loading condition, the maximum deformation was approximately 2.8 times lower than in the transverse case (127.88 mm versus 358.55 mm). Nevertheless, the combined catenary-curved and CS configuration (R100-6.6g-c-CS) reduced u_{max} from 127.88 to 79.06 mm (Figure 15c,d), representing an overall reduction of 38.2% (Table 5), thereby further increasing the global stiffness of the body structure and improving passive safety.

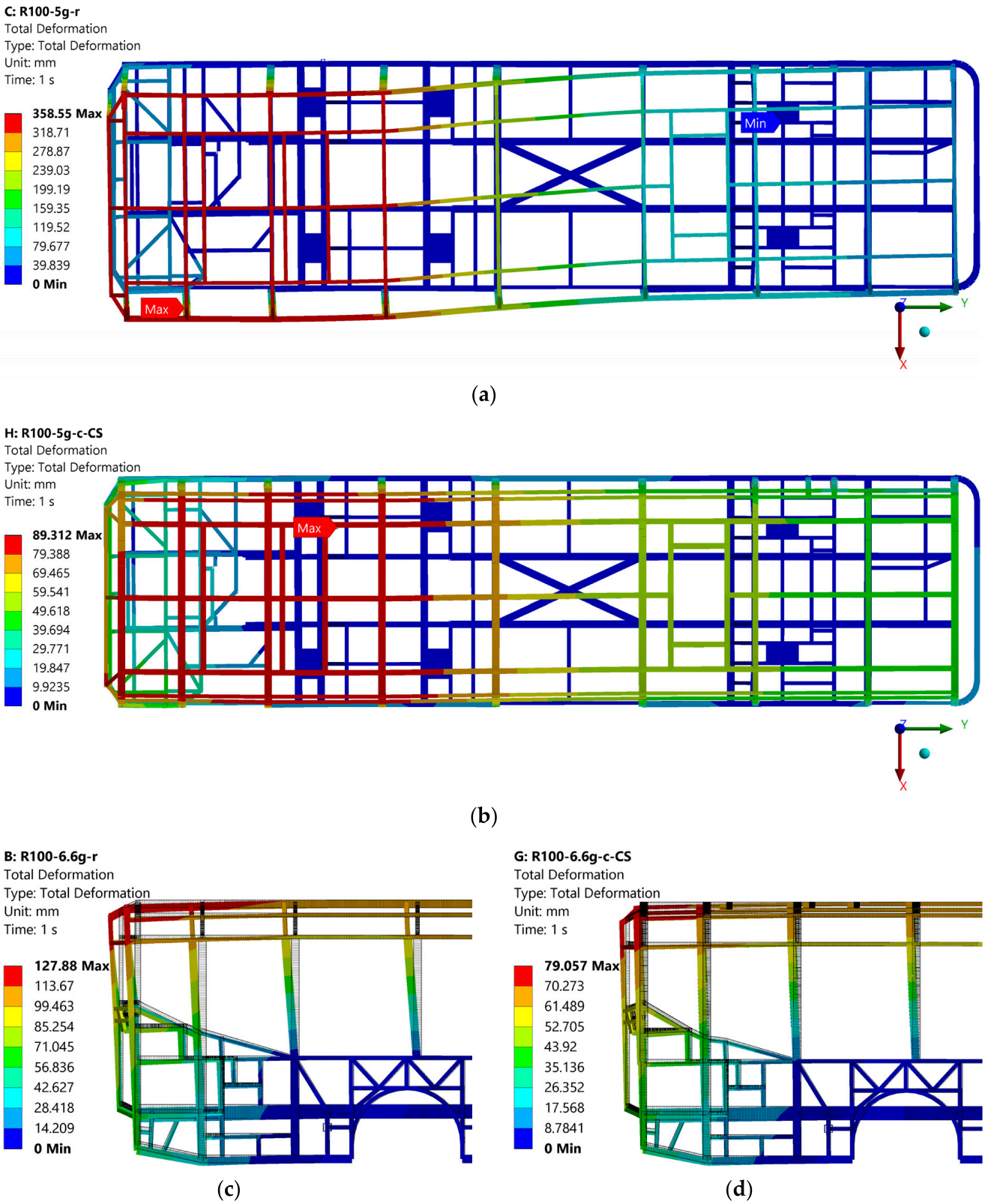


Figure 15. Deformation maps under R100 loading: (**a**) R100-5g-r. (**b**) R100-5g-c-CS. (**c**) R100-6.6g-r. (**d**) R100-6.6g-c-CS.

3.3. Cable-Force and Anchorage Assessment

The mechanical response of the CS joints was additionally evaluated using the Spring Probe results in Ansys Mechanical. In the D-2g-CS model, the axial cable forces ranged from 4.835 to 10.380 kN, corresponding to cable stresses of approximately 96.2–206.5 MPa

for the adopted 8 mm cable diameter. In the R100-6.6g-c-CS model, the forces varied within a substantially narrower range of 5.878–6.385 kN, whereas in the R100-5g-c-CS model they ranged from 5.668 to 6.707 kN, corresponding to maximum cable stresses of approximately 127.0 and 133.4 MPa, respectively. In all investigated cases, the cable force remained positive; therefore, complete slackening of the tension-only CS joints was not observed. In the adopted idealized global longitudinal-joint representation, the axial cable force is transmitted directly to the end anchorages. The maximum force obtained from the baseline D-2g-CS analysis at T_0 = 6000 N was therefore subsequently used as the loading input for the dedicated component-level anchorage assessment described below.

The component-level anchorage analysis showed that the maximum equivalent von Mises stress under the applied cable force of 10.38 kN reached 197.87 MPa (Figure 16a). The peak was localized at the perimeter weld connecting the anchorage base plate to the RHS member rather than at the cable-attachment hole (Figure 16a). This value remained below the yield strength of the adopted S235 material, corresponding to a minimum safety factor of 1.28. By comparison, the maximum equivalent stress in the lug plate was 87.07 MPa and occurred locally at the edge of the 12 mm pin hole (Figure 16b).

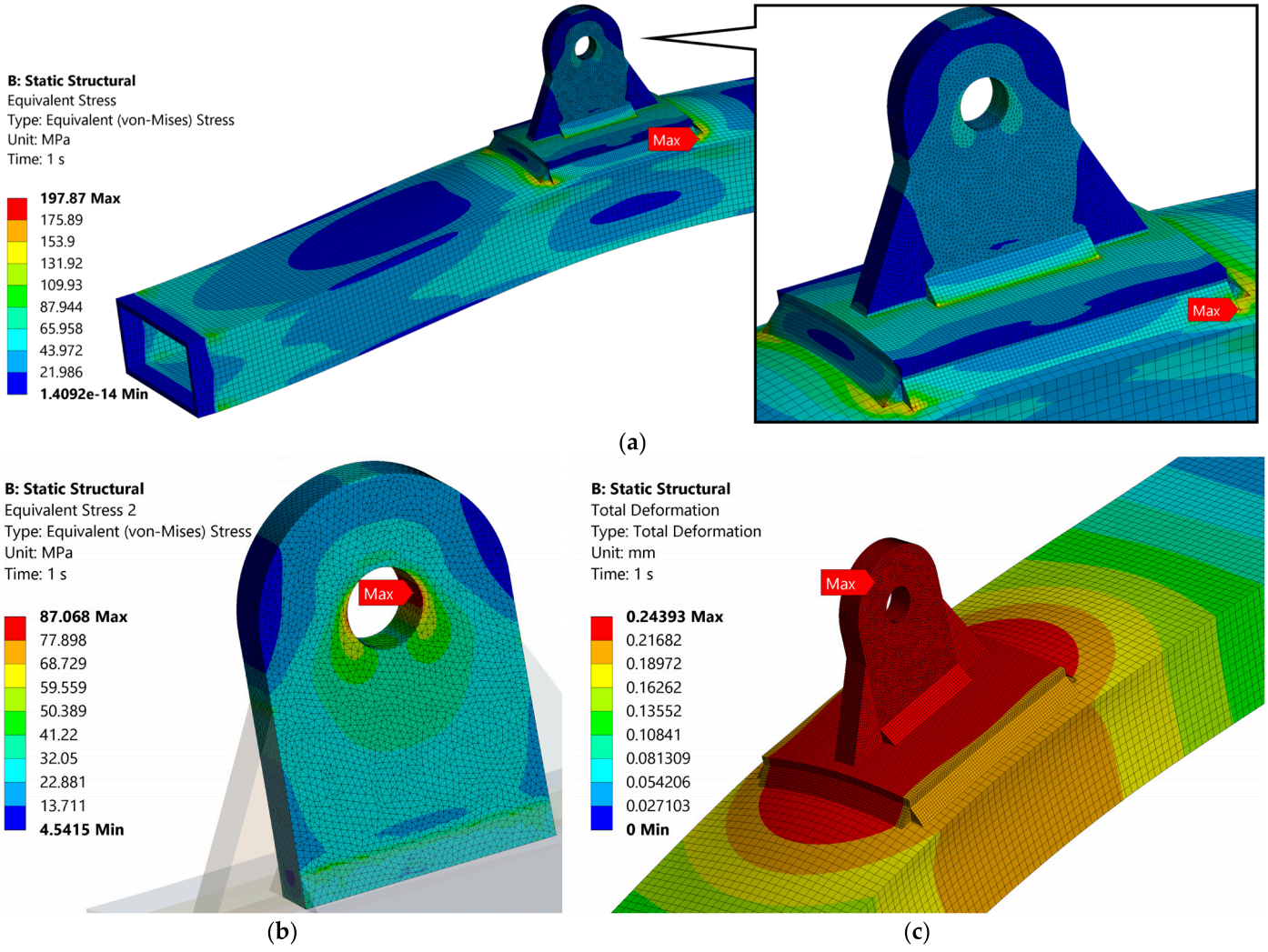


Figure 16. Results of the component-level finite-element analysis of the representative CS anchorage: (**a**) global equivalent stress distribution with local stress concentration in the welded support region; (**b**) stress distribution in the lug plate; (**c**) total deformation.

The maximum total deformation of the anchorage assembly was only 0.244 mm and occurred in the upper lug region (Figure 16c). In addition, the maximum equivalent stress increased essentially proportionally with the applied load, from 39.58 MPa at 20% of the final load to 79.15, 138.51, and 197.87 MPa at 40%, 70%, and 100%, respectively, indicating an elastic structural response throughout the investigated loading interval.

These results indicate that the proposed representative anchorage is capable of transferring the maximum cable force obtained from the baseline D-2g-CS model at T_0 = 6000 N without predicted static yielding or excessive local deformation. The critical load-transfer region is the base-plate-to-tube welded connection, whereas neither the lug plate nor the pin-hole region governs the static response.

3.4. Serviceability and Cable-Layout Screening Under Diagonal Racking

To complement the strength and fatigue assessment with a serviceability-oriented indicator, the in-plane distortion of the three passenger-door openings was quantified from the relative change in their two diagonals. Two longitudinal Spring Joints were introduced across each opening: F1 and F2 for the front door, M1 and M2 for the middle door, and R1 and R2 for the rear door (Figure 17). These joints were used solely as numerical measuring elements. Their longitudinal stiffness was set to 1.0×10^{-4} N/mm, with zero preload and damping, so that their contribution to the structural stiffness was negligible. Even for the largest measured diagonal change of 16.94 mm, the corresponding spring force does not exceed 1.7×10^{-3} N and therefore cannot materially affect the calculated response of the bus body.

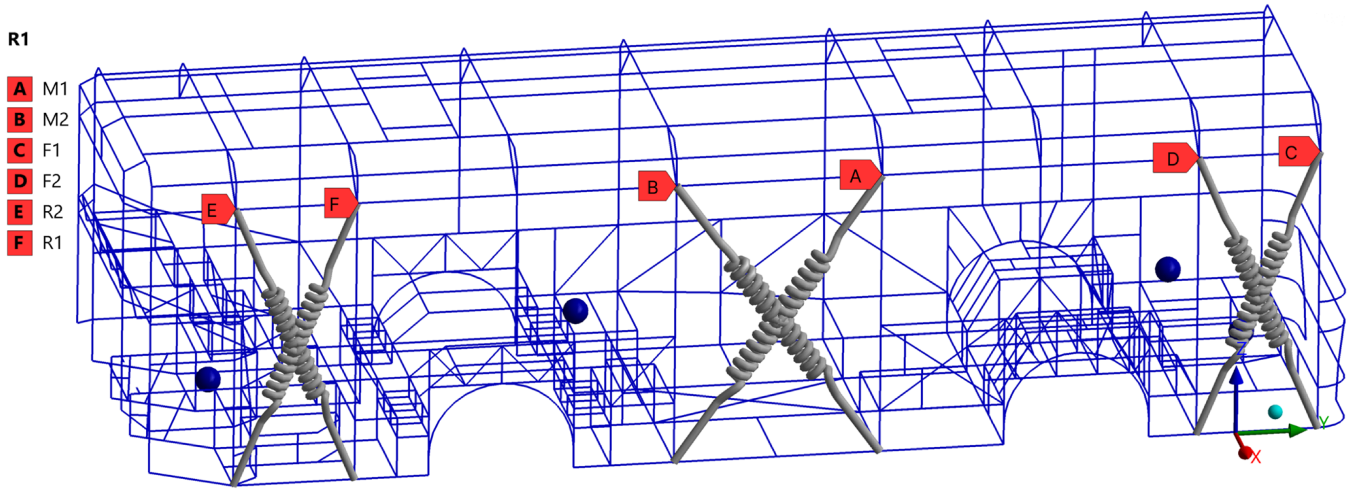


Figure 17. Numerical scheme for quantifying door-opening distortion using low-stiffness diagonal Spring Joints: F1–F2, front door; M1–M2, middle door; R1–R2, rear door.

The signed changes in diagonal length are presented in Table 6. In each door opening, the two diagonals changed in opposite directions and with similar magnitudes, indicating predominantly racking-type distortion rather than uniform expansion or contraction of the opening. More importantly, the absolute magnitude of the diagonal change decreased for all six monitored diagonals after introduction of the CS reinforcement.

Table 6. Changes in the door-opening diagonal lengths for the reference and CS-reinforced configurations.

Metric	Measurement/Opening	D-2g, mm	D-2g-CS, mm	Reduction, %
Diagonal change Δl	F1—front door	−4.65	−2.98	35.88
	F2—front door	4.60	2.92	36.55
	M1—middle door	16.91	14.18	16.18
	M2—middle door	−16.94	−14.26	15.81
	R1—rear door	3.73	3.30	11.40
	R2—rear door	−3.69	−3.30	10.60
Door-opening racking D_op	Front door	9.25	5.90	36.22
	Middle door	33.85	28.44	15.99
	Rear door	7.42	6.60	11.01
Overall six-diagonal mean |Δl|	All six diagonals	8.42	6.82	18.97

For a door-opening-level comparison, the distortion may be represented by a simple racking indicator defined from the signed changes of its two diagonals:

$$D_{\mathrm{op}} = |\Delta l_1 - \Delta l_2|, \tag{16}$$

where Δl_1, Δl_2—changes in the lengths of the two diagonals of the corresponding door opening, mm; D_{op}—door-opening racking indicator, mm. Because the two diagonals change in opposite directions in all investigated cases, D_{op} is also equal to the sum of their absolute changes.

The relative reduction due to the CS reinforcement is then

$$\eta_D = \frac{D_{\mathrm{op,D-2g}} - D_{\mathrm{op,D-2g-CS}}}{D_{\mathrm{op,D-2g}}} \times 100\%, \tag{17}$$

where η_D—reduction in the door-opening racking indicator, %.

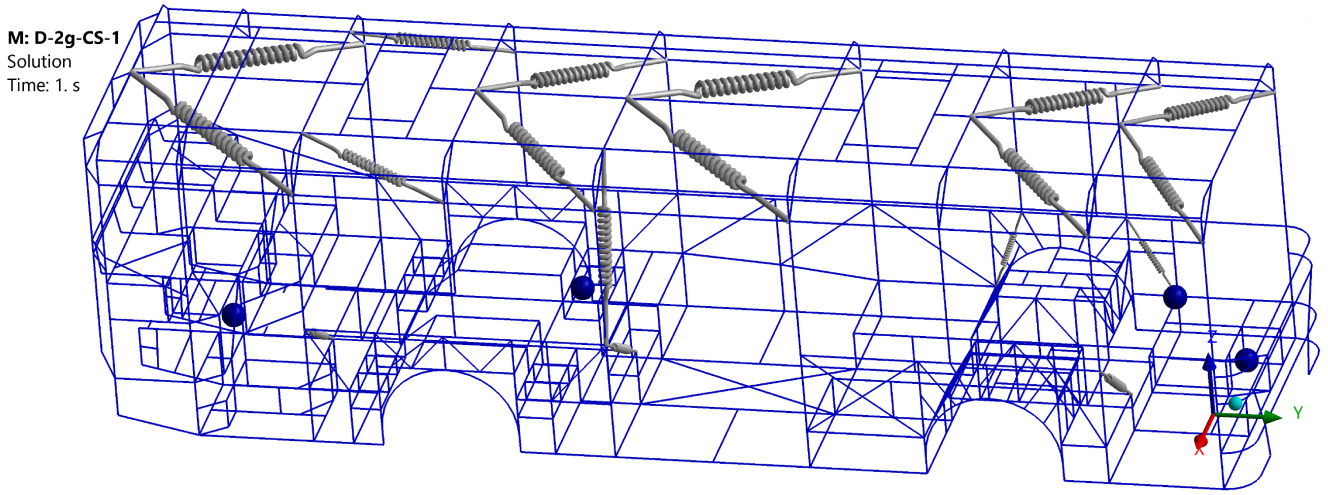
The front-door opening exhibited the largest relative improvement. Its racking indicator decreased from 9.25 mm in D-2g to 5.90 mm in D-2g-CS, corresponding to a reduction of 36.22%. The middle door showed the largest absolute distortion in both configurations: D_{op} decreased from 33.85 to 28.44 mm, or by 15.99%. The rear-door opening was less distorted in absolute terms and exhibited a reduction from 7.42 to 6.60 mm, corresponding to 11.01%.

Thus, the CS system improved the in-plane dimensional stability of all three door openings, although the magnitude of the effect was spatially non-uniform. The strongest stabilization occurred at the front door, whereas the middle opening remained the serviceability-governing region despite the reduction obtained with the reinforced configuration. This distinction is relevant because global stress or deformation measures alone do not necessarily quantify local aperture distortion, which directly affects the dimensional stability of door mounting and closure interfaces.

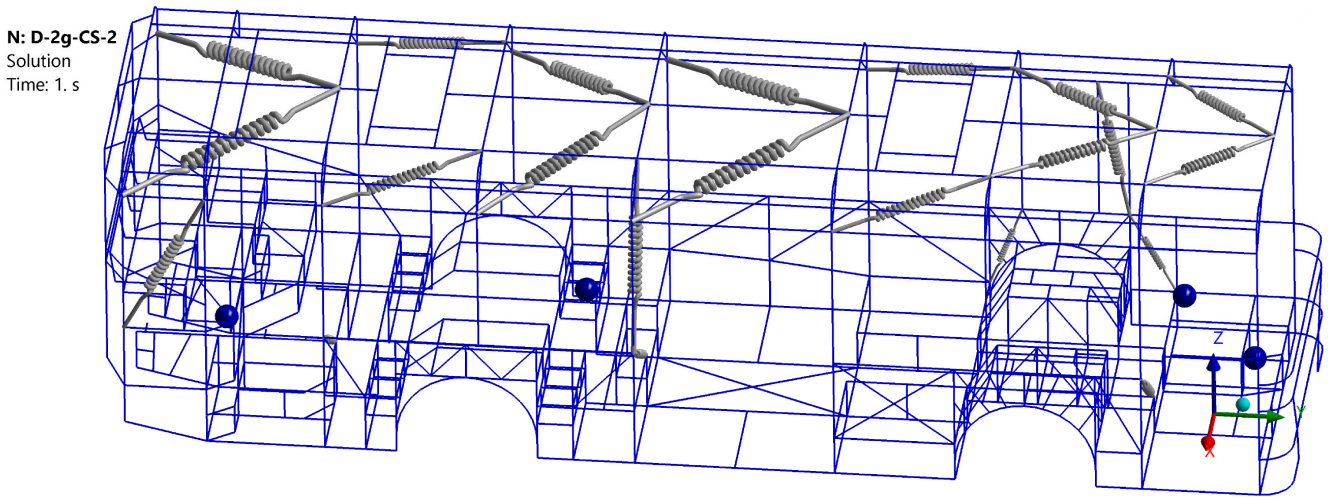
The consistency of the two diagonal measurements provides an additional check on this conclusion. For the front opening, the reductions calculated independently from F1 and F2 were 35.88 and 36.55%, respectively; for the middle opening, 16.18 and 15.81%; and for the rear opening, 11.40 and 10.60%. The close agreement within each pair indicates that the calculated improvement is associated with a systematic reduction in opening racking rather than with a local displacement anomaly at a single measurement point. Considering all six diagonals together, the mean absolute diagonal change decreased from 8.420 to 6.823 mm, corresponding to an overall reduction of approximately 18.97%.

No manufacturer-specific admissible limit for door-opening diagonal distortion was imposed in the present study. The obtained values are therefore interpreted comparatively rather than as a pass/fail serviceability criterion. Nevertheless, the results provide a direct quantitative measure of aperture stability and complement the global strength and fatigue indicators by demonstrating that the CS reinforcement also reduces local deformation of functional body openings.

To provide an additional quantitative indication of the layout-screening process, two representative one-directional CS configurations were re-evaluated under the same D-2g loading conditions and compared with the retained criss-cross D-2g-CS arrangement (Figure 18). In D-2g-CS-1, where the CS diagonals were predominantly inclined opposite to the direction of vehicle travel, the maximum von Mises stress was 302.24 MPa, the average von Mises stress was 40.25 MPa, and the maximum total deformation was 98.07 mm. For the opposite diagonal orientation, D-2g-CS-2, where the CS diagonals were predominantly inclined in the direction of vehicle travel, the corresponding values were 300.89 MPa, 39.50 MPa, and 96.34 mm, respectively.



(**a**)



(**b**)

Figure 18. Representative one-directional CS layouts used for verification of the numerical screening procedure: (**a**) D-2g-CS-1, with Cable Spring diagonals predominantly inclined opposite to the direction of vehicle travel; (**b**) D-2g-CS-2, with Cable Spring diagonals predominantly inclined in the direction of travel.

The retained criss-cross D-2g-CS configuration produced lower values for all three response measures: 298.70 MPa maximum von Mises stress, 38.68 MPa average stress, and 91.94 mm maximum total deformation. Relative to D-2g-CS-2, the criss-cross arrangement reduced the maximum stress by approximately 0.73%, the average stress by 2.08%, and the maximum deformation by 4.57%. Relative to D-2g-CS-1, the corresponding reductions were approximately 1.17%, 3.90%, and 6.25%. Thus, although both one-directional layouts provided substantial reinforcement relative to the unreinforced D-2g body, the criss-cross arrangement produced the most favourable combined stress and deformation response among the representative layouts reported here.

This comparison also illustrates why the cable arrangement itself constitutes an important design variable. Under diagonal racking, the deformation of the spatial body frame does not occur uniformly in a single direction; consequently, a one-directional set of tension-only members cannot provide the same degree of restraint for both senses of local frame distortion. The criss-cross arrangement provides complementary diagonal load paths and therefore allows the prestressed cable system to participate more effectively in the redistribution of racking-induced forces over the roof and sidewall structure. These representative results support the selection of the D-2g-CS layout used in the analyses reported above, while they should not be interpreted as proof of a mathematically global optimum.

4. Discussion

The numerical results demonstrate that prestressed Cable Spring (CS) joints can improve the structural efficiency of a tubular bus body through two complementary mechanisms: the elastic resistance from cable elongation and the geometric stiffness from initial pretension. Unlike additional steel braces, cables primarily act in tension and can be routed through otherwise unused hollow members or concealed beneath the interior lining. Consequently, the proposed system increases stiffness without substantially changing the external geometry, passenger-compartment layout, or basic manufacturing architecture of the body frame. From an engineering perspective, the proposed concept can be integrated into existing tubular bus-body manufacturing technology with minimal changes to the basic frame architecture, while enabling post-assembly pretension adjustment, inspection, replacement, and structural health monitoring of the reinforcing elements.

Under diagonal racking, the CS reinforcement produced a substantial reduction in global deformation and average stress, whereas the decrease in the peak local stress was considerably smaller. The difference between the reductions in average and maximum stress indicates that the principal contribution of the cable system is not the elimination of the most highly stressed local joint, but the redistribution of loads over a larger portion of the spatial frame. The increase in the average safety factor from 8.86 to 9.77 further confirms that the structure became more uniformly loaded. The displacement at the critical engine mounting point decreased from 73.61 mm to 54.77 mm, indicating that CS joints may also improve the dimensional stability of powertrain, door, glazing and suspension interfaces.

The pretension sensitivity study further clarifies the role of the initial cable force in the structural response. Increasing T_0 from 3000 to 9000 N changed the maximum total deformation by only 2.0%, while the average von Mises stress varied by approximately 1.1% across the investigated range. Taken together with the analytical formulation in Equations (8)–(13), these results suggest that, within the investigated pretension range, the primary reinforcement effect is associated with the additional tension-only load paths and the elastic axial stiffness of the cables, whereas pretension provides a secondary geometric-stiffening and tuning contribution. The non-monotonic variation of the maximum local

von Mises stress further indicates that increasing pretension does not necessarily produce a proportional reduction in peak stress. Consequently, selection of the final pretension level should account not only for global stiffness but also for local stress redistribution, cable forces, anchorage loading, fatigue, and serviceability requirements.

The lightweighting effect can be evaluated directly from the masses of the investigated finite-element body-frame configurations. The conventional rectangular steel frame has a mass of 2312.2 kg, whereas the catenary-curved frame has a mass of 1936.0 kg, corresponding to a reduction of 376.2 kg (16.3%). Despite its lower structural mass, the catenary-curved configuration exhibited lower stress and deformation levels than the conventional rectangular frame, with further improvements achieved after the integration of CS joints. This additional structural reserve suggests that, at an equivalent stress level, further mass reduction in the catenary-curved CS-reinforced frame may be theoretically achievable through additional structural optimisation of the body frame. Interestingly, the observed 16.3% frame-mass reduction is very close to the 16.2% reduction in average von Mises stress obtained after CS integration under diagonal racking. Although these values originate from different structural comparisons and cannot establish a general relationship, their close agreement suggests a hypothesis for future investigation that relative average-stress reduction may serve as an indicator of achievable mass reduction during structural optimization. The mass penalty of the CS system itself is comparatively small: for the CS-model, 29 steel cables of 8 mm diameter and approximately 2 m representative length correspond to about 22.9 kg. The final net mass saving should additionally account for the anchorage components and requires dedicated structural optimization under equivalent strength and stiffness constraints. This demonstrated reduction in steel-frame mass provides a direct quantitative sustainability benefit by reducing structural material use.

The proposed concept demonstrated its highest effectiveness under the UNECE R100 transverse 5 g loading condition. It should be noted that the catenary-curved geometry and CS reinforcement are intentionally coupled in the R100 models, since the proposed concept relies on their combined bow–bowstring action; therefore, a rectangular configuration with CS reinforcement would not reproduce the same prestressing mechanism. The results indicate that the principal advantage of CS joints is achieved when the plane of the CS and the inter-window pillars coincides with the dominant deformation plane, thereby converting racking or bending deformation into axial cable tension. The lower effectiveness observed under the longitudinal 6.6 g loading condition further confirms that the structural contribution of the CS system depends strongly on the loading direction.

The comparison of the three loading cases demonstrates a pronounced directional dependence of the CS reinforcement effect. Under diagonal racking, the distributed CS joints primarily increase global frame stiffness and promote load redistribution throughout the spatial structure. Under transverse 5 g loading, the reinforcement is most effective because the inertial forces act predominantly in the plane of the catenary-curved inter-window pillars and their prestressed cables, directly activating the bow–bowstring load-carrying mechanism. In contrast, under longitudinal 6.6 g loading, the dominant forces act largely outside this plane, and the same mechanism is therefore activated less efficiently. Thus, the effectiveness of CS reinforcement depends not only on cable stiffness and pretension but also on the alignment between the reinforced structural plane and the dominant deformation mode.

In the reference R100-5g-r model, regions with ($SF < 1$) developed near both ends of several inter-window pillars, indicating local yielding and the initiation of plastic-hinge mechanisms. Once such hinges form, the sidewall progressively loses its original geometry and load-carrying capability. In the R100-5g-c-CS model, these critical regions were

almost completely eliminated from the rear inter-window pillars and the maximum stress shifted from the sidewall to the rear-seat support frame. This migration of the critical location indicates that the sidewall ceased to govern the global failure mechanism. The larger reduction in global deformation than in maximum stress reflects the fact that CS reinforcement primarily increases overall frame stiffness and redistributes loads, while the peak stress remains governed by localized stress concentrations. Although the maximum stress of 281.23 MPa and the minimum safety factor of 0.90 indicate highly localized yielding in the rear-seat support frame, the affected region occupies only a small portion of the member, as shown in Figure 13b, and does not indicate yielding of the entire cross-section or a significant loss of member stiffness or geometry. Such localized overstress can be considered acceptable at the present conceptual design stage; if required, it can be further reduced by local reinforcement or the use of higher-strength steel. The result is particularly relevant to rollover safety because UN Regulation No. 66 evaluates the strength of bus superstructures and the preservation of the residual survival space during rollover. This concept shows considerable potential to improve bus body structures designed to meet the structural requirements of UNECE Regulations Nos. 14, 66, 80, 100 and 110. The use of prestress also enables tuning of the completed body after welding and assembly. Manufacturing tolerances, welding distortion and asymmetric equipment installation may produce an initially non-uniform stiffness distribution. Controlled cable tension could partially compensate for these deviations and equalize the deformation response of the left and right sidewalls. In a more advanced implementation, individually adjustable CS joints could be used as passive structural tuning elements, with the target pretension determined from measured body-frame deformation rather than assigned solely from nominal design geometry. Integration of strain-gauge-based cable-force monitoring could transform the proposed CS joints into elements of a structural health-monitoring system capable of detecting pretension loss, structural damage, and overload events.

However, the introduction of prestressed cables creates several design and maintenance challenges. Cable force may decrease because of seating of the end fittings, local embedment, strand relaxation, thermal cycling, vibration, corrosion, or permanent deformation of the anchorage regions. Insufficient tension would permit slack, impact loading, fretting and possible noise, whereas excessive pretension could introduce unnecessary initial stresses into the pillars and welded joints. The required pretension tolerance must therefore be defined as a permissible operating interval rather than as a single nominal value. The service schedule should include tension verification after the initial running-in period and subsequently during periodic maintenance. Adjustment can be performed using a turnbuckle, threaded tensioner, calibrated torque procedure, or direct force measurement.

The component-level analysis confirms that the anchorage represents an important local load-transfer region, but also demonstrates that a practically realizable welded configuration can sustain the maximum cable force obtained from the global model without predicted static yielding. The highest stress was transferred away from the lug hole and localized at the base-plate perimeter weld, where the minimum safety factor remained above unity. This result supports the mechanical feasibility of the CS concept while also identifying the welded base connection as the principal region requiring attention during detailed design. The present component-level assessment addresses the static strength of the anchorage; the fatigue screening presented in this study concerns the global body-frame response and should not be interpreted as a weld-detail fatigue assessment of the anchorage.

The screening-level fatigue assessment presented above provides an initial comparative indication of the influence of CS reinforcement; however, a complete fatigue-life

evaluation requires representative cyclic road-load histories. The present study considers severe quasi-static and inertial loading cases, whereas an operating bus experiences millions of lower-amplitude cycles caused by road irregularities, cornering, braking, suspension articulation and body vibration [127–129]. Prestress may be beneficial by keeping the cable continuously active and preventing load reversals, but fluctuating tension may initiate fatigue damage at strand terminations and threaded fittings. The influence of prestressing on fatigue should not, however, be interpreted solely in terms of the initial tensile stress. In the tubular frame, cable pretension modifies the initial stress state but also redistributes the stresses induced by external loading; therefore, the resulting stress amplitude and stress range may be lower than in the corresponding structure without CS reinforcement, potentially improving fatigue performance. For the cables and their anchorage points, the tensile mean stress introduced by pretension remains an important fatigue parameter and must be considered together with the alternating stress amplitude. Consequently, quantitative assessment of fatigue performance requires analysis of the complete cyclic stress history rather than the prestress level alone. Experimental validation would be required to determine the allowable cable-tension range, pretension loss, endurance of the end fittings, and sensitivity to installation tolerances under representative service loading. Consequently, the screening-level fatigue results obtained here should be interpreted as a comparative assessment under a severe constant-amplitude loading envelope rather than as a prediction of the actual operational fatigue life of the bus. A full service-life assessment would require measured or experimentally validated cyclic road-load histories, including road roughness, braking, cornering, suspension articulation, vibration, and pretension-loss effects.

The current finite-element results should be interpreted within the limitations of the adopted numerical model. Although the mesh-sensitivity analysis confirmed consistently high mesh-quality metrics across the investigated discretizations, experimental validation of the proposed CS-reinforced bus body has not yet been performed. Consequently, the numerical results should primarily be interpreted as a comparative assessment of the investigated structural configurations rather than as experimentally validated absolute predictions. The tubular body was represented by BEAM188 elements, the floor sheet panels by SHELL181 elements, and the cables were idealized as tension-only longitudinal joints with prescribed stiffness and pretension. This approach is appropriate for evaluating global load redistribution but does not fully reproduce local contact, cable bending over guides, friction, anchorage deformation, strand construction, joint clearances, weld details, or progressive cable failure. The selected cable layout was obtained from more than twenty numerical variants, but it cannot yet be regarded as a global optimum.

Future work should extend the present component-level static anchorage assessment toward fully nonlinear detailed modelling of the tubular members and cable anchorages, combined with component and full-body experiments. The numerical model should include geometric nonlinearity, contact and friction, pretension losses, temperature effects, local anchorage flexibility, cable rupture and post-yield behaviour of the surrounding frame. Future studies should therefore focus on local, region-specific optimization of the CS system, since different parts of the bus body may require different reinforcement levels. In some structural regions, a pretension of approximately 3000 N may already provide sufficient stiffness enhancement, whereas more highly loaded areas may benefit from pretension levels approaching 9000 N, potentially in combination with larger-diameter cables. Such a differentiated design approach could improve structural efficiency while avoiding unnecessary cable mass, pretension, and anchorage loading in less critical regions.

Overall, the study indicates that CS joints are most valuable not as direct substitutes for all tubular members, but as selectively positioned tension-only load paths that suppress racking, redistribute stresses and delay the formation of plastic mechanisms. Their greatest potential lies in large openings and highly deformable sections of bus bodies where rigid triangulation is geometrically or functionally impractical. The reductions in deformation observed under diagonal racking and UNECE R100 loading justify further development toward experimentally validated, inspectable, replaceable, and potentially sensor-equipped cable reinforcement systems.

5. Conclusions

The conducted research allows the following main conclusions to be drawn:

1. The proposed Cable Spring (CS) concept effectively increases the global stiffness of the bus body by introducing additional tension-only load paths that redistribute internal forces through both elastic cable action and geometric stiffening induced by pretension. Unlike conventional steel reinforcements, the proposed solution introduces lightweight tension-only load paths that can be routed through tubular members or concealed beneath the interior lining while preserving the external geometry and functional layout of the passenger compartment.
2. Under diagonal racking loading, the integration of CS joints at the baseline pretension of 6000 N reduced the maximum total deformation by 28.4% and the average von Mises stress by 16.2%, while increasing the average safety factor by 10.3%. The improved load redistribution also reduced deformation at the selected powertrain mounting point and indicates additional structural reserve for future optimization of the body frame. A pretension sensitivity analysis over the range of 3000–9000 N showed that the maximum total deformation varied by only 2.0% and the average von Mises stress by approximately 1.1%, while substantial reductions relative to the non-reinforced model were maintained at all investigated pretension levels. This confirms that the global reinforcement effect is not dependent on the single baseline pretension value. The additional screening assessments also showed improved serviceability of the powertrain and door-opening interfaces, an 86.3% increase in the minimum predicted fatigue life under the adopted constant-amplitude loading envelope, and elastic static load transfer through the representative CS anchorage under the baseline maximum cable force.
3. Under the UNECE R100 transverse (5 g) loading condition, the combined catenary-curved and CS configuration demonstrated the greatest effectiveness, reducing the maximum equivalent stress, average equivalent stress, and maximum total deformation by 41.2%, 24.7%, and 75.1%, respectively, relative to the rectangular reference model. The redistribution of stresses largely eliminated the regions of local yielding within the inter-window pillars and transferred the critical stress location away from the passenger sidewall, contributing to improved preservation of the overall structural integrity and body-frame geometry.
4. The effectiveness of the proposed reinforcement depends on the loading direction and structural load paths. The substantially greater improvement obtained under transverse loading confirms that the catenary-curved pillar with an internal prestressed cable behaves as a bow–bowstring structural system, indicating that the layout, pretension, and anchorage of CS joints should be optimized according to the dominant loading conditions of individual body regions.
5. The investigated structural concept provides a quantitative lightweighting benefit at the body-frame level: the mass of the catenary-curved steel frame is 16.3% lower than that of the conventional rectangular configuration, while maintaining a more

favourable structural response. Accordingly, the demonstrated sustainability benefit is primarily associated with reduced use of structural materials, whereas further mass reduction through structural optimisation remains a subject for future research. The potential for concealed installation, modularity, and structural health monitoring via cable-force sensing may also make the CS concept potentially applicable to a broader range of future bus structures, including autonomous platforms designed to meet the structural requirements of UNECE Regulations Nos. 14, 66, 80, 100, and 110; however, vehicle-level benefits associated specifically with autonomous operation were not evaluated in the present study.

Author Contributions: Conceptualization, K.H.; methodology, K.H.; software, K.H.; validation, K.H.; formal analysis, K.H., O.D., M.G. and L.N.; investigation, K.H., O.D., M.G. and L.N.; resources, K.H.; data curation, K.H., O.D., M.G. and L.N.; writing—original draft preparation, K.H.; writing—review and editing, K.H., O.D., M.G. and L.N.; visualization, K.H.; supervision, K.H., O.D., M.G. and L.N.; project administration, M.G. and L.N.; funding acquisition, M.G. and L.N. All authors have read and agreed to the published version of the manuscript.

Funding: This research received no external funding.

Institutional Review Board Statement: Not applicable.

Informed Consent Statement: Not applicable.

Data Availability Statement: Dataset available on request from the authors.

Conflicts of Interest: The authors declare no conflicts of interest.

References

1. Viana-Fons, J.D.; Payá, J. Dynamic cabin model of an urban bus in real driving conditions. *Energy* **2024**, *288*, 129769. [CrossRef]
2. Kepka, M.; Kepka, M.; Minich, R. A case study on fatigue life assessment of an electric bus bodywork. *Int. J. Fatigue* **2024**, *179*, 108040. [CrossRef]
3. Thamsuwan, O.; Blood, R.P.; Ching, R.P.; Boyle, L.; Johnson, P.W. Whole body vibration exposures in bus drivers: A comparison between a high-floor coach and a low-floor city bus. *Int. J. Ind. Ergon.* **2013**, *43*, 9–17. [CrossRef]
4. Wu, Z.; Zhou, H.; Xi, H.; Wu, N. Analysing public acceptance of autonomous buses based on an extended TAM model. *IET Intell. Transp. Syst.* **2021**, *15*, 1318–1330. [CrossRef]
5. Čudina Ivančev, A.; Džambas, T.; Dragčević, V. The Impact of Autonomous Vehicles on the Transportation Network with a Focus on the Physical Road Infrastructure. *Infrastructures* **2025**, *10*, 347. [CrossRef]
6. Chatterjee, S.; Majumder, A. Enhancing Vehicle Safety: An Arduino-Based Real-Time Collision Avoidance System Using Ultrasonic Sensors and Warning Alerts. In Proceedings of the 2025 International Conference on Electronics, AI and Computing (EAIC), Jalandhar, India, 5–7 June 2025; pp. 1–9. [CrossRef]
7. Burchart, D.; Przytuła, I. Sustainability Assessment Methods for the Transport Sector Considering the Life Cycle Concept—A Review. *Sustainability* **2024**, *16*, 8148. [CrossRef]
8. Lan, F.; Chen, J.; Lin, J. Comparative analysis for bus side structures and lightweight optimization. *Proc. Inst. Mech. Eng. Part D J. Automob. Eng.* **2004**, *218*, 1067–1075. [CrossRef]
9. Pasaulis, T.; Pečeliūnas, R.; Žuraulis, V.; Raudonis, V.; Sledevič, T.; Matuzevičius, D. Cross-Dataset Insights for Fine-Grained Vehicle Orientation Prediction. *Electronics* **2026**, *15*, 2097. [CrossRef]
10. Klimenko, I.; Kalivoda, J.; Neduzha, L. Parameter optimization of the locomotive running gear. In Proceedings of the 22nd International Scientific Conference Transport Means, Trakai, Lithuania, 3–5 October 2018; pp. 1095–1098.
11. Wang, Y.; Yang, J.; Chen, Y.; Ma, X.; Chen, Y. Experimental Design and Practice of Vehicle Cabins Based on Passenger Comfort Evaluation. *Appl. Sci.* **2026**, *16*, 4965. [CrossRef]
12. Wang, J.; Chen, J.; Zhang, Y.; Lan, F.; Zhou, Y. Active-Learning Reliability Analysis of Automotive Structures Based on Multi-Software Interaction in the MATLAB Environment. *Appl. Sci.* **2024**, *14*, 5452. [CrossRef]
13. Klimenko, I.; Černiauskaite, L.; Neduzha, L.; Ochkasov, O. Mathematical simulation of spatial oscillations of the "Underframe-Track" system interaction. In Proceedings of the 12th International Conference Intelligent Technologies in Logistics and Mechatronics Systems—ITELMS'2018, Panavezys, Lithuania, 26–27 April 2018; pp. 105–114.

14. Lunys, O.; Neduzha, L.; Tatarinova, V. Stability research of the main-line locomotive movement. In Proceedings of the 23rd International Conference Transport Means, Palanga, Lithuania, 2–4 October 2019; pp. 1341–1345.
15. Zhang, Y.; Xu, N.; Yin, Z.; Guo, K. Tire capacity based vehicle stability evaluation framework for adaptive coordination of trajectory tracking and vehicle stability control. *Proc. Inst. Mech. Eng. Part D J. Automob. Eng.* **2026**, 09544070261468274. [CrossRef]
16. Sulym, A.; Khozia, P.; Tretiak, E.; Píštěk, V.; Fomin, O.; Kučera, P. Aspects of Strength Testing of Tank Containers in Compliance with the Requirements of the UN Navigation Rules and Regulations. *J. Mar. Sci. Eng.* **2021**, *9*, 349. [CrossRef]
17. Hu, L.; Lu, T.; Li, G.; Zhang, X.; Cai, H. Automatic Generation of Intelligent Vehicle Testing Scenarios at Intersections Based on Natural Driving Datasets. *IEEE Trans. Intell. Veh.* **2024**, *9*, 5448–5460. [CrossRef]
18. Meilus, L.; Maskeliūnaitė, L.; Sivilevičius, H. Determining the Significance of Criteria Quality of Passengers Railway Traction Using Expert Evaluation Methods. In *Reliability and Statistics in Transportation and Communication: Human Sustainability and Resilience in the Digital Age. RelStat 2024*; Kabashkin, I., Yatskiv, I., Prentkovskis, O., Eds.; Lecture Notes in Networks and Systems; Springer: Cham, Switzerland, 2025; Volume 1337. [CrossRef]
19. Tiutkin, O.; Neduzha, L.; Kalivoda, J. Finite-element analysis of strengthening the subgrade on the basis of boring and mixing technology. *Transp. Probl.* **2021**, *16*, 189–197. [CrossRef]
20. Deco, A.; Tidwell, Z.; Jarecki, W. Advancing the Development of Condition-Based Maintenance for Commercial Transport Aircraft Structure. *E-J. Nondestruct. Test.* **2026**, *31*, 1–8. [CrossRef]
21. Sulym, A.; Bialobrzheskyi, O.; Khozia, P.; Lomonos, A. Saving energy resources during operation of rolling stock of underground electrified transport. *Nauk. Visnyk Natsionalnoho Hirnychogo Universytetu* **2024**, *5*, 65–70. [CrossRef]
22. Petrea, M.; Gheorghe, C.; Soica, A. Accessibility in Bus-Based Public Transport Across European Cities: A Bibliometric and Thematic Review of Bus Stop and Station Infrastructure for Inclusive Urban Mobility. *Urban Sci.* **2026**, *10*, 399. [CrossRef]
23. Ižvolt, L.; Dobeš, P.; Papánová, Z.; Mečár, M. Experimental Monitoring of Dynamic Parameters of the Sub-Ballast Layers as a Prerequisite for a High-Quality and Sustainable Railway Line. *Sustainability* **2024**, *16*, 2229. [CrossRef]
24. Bondarenko, I.; Lukoševičius, V.; Keršys, R.; Neduzha, L. Innovative Trends in Railway Condition Monitoring. *Transp. Res. Procedia* **2024**, *77*, 10–17. [CrossRef]
25. Ji, X.; Koue, J.; Zhang, R.; Hirayama, K. Monitoring and service for ships from the perspective of the remote operations center. *J. Shipp. Trd.* **2026**, *11*, 20. [CrossRef]
26. Werbińska-Wojciechowska, S.; Giel, R.; Winiarska, K. Digital Twin Approach for Operation and Maintenance of Transportation System—Systematic Review. *Sensors* **2024**, *24*, 6069. [CrossRef]
27. Kose, N.A.; Kose, K.; Liang, F. From Concrete to Code: A Survey of AI-Driven Transportation Infrastructure, Security, and Human Interaction. *Sensors* **2026**, *26*, 2219. [CrossRef]
28. Ersöz, O.Ö.; İnal, A.F.; Aktepe, A.; Türker, A.K.; Ersöz, S. A Systematic Literature Review of the Predictive Maintenance from Transportation Systems Aspect. *Sustainability* **2022**, *14*, 14536. [CrossRef]
29. Nedeliaková, E.; Valla, M.; Masár, M. Modernization of Railway Wagons for Customer Satisfaction and Safety. *Vehicles* **2024**, *6*, 374–383. [CrossRef]
30. Alizhan, A.; Apshikur, B.; Alimkulov, M.; Goltsev, A.; Chernavin, V.; Almas, K. Dynamic Behavior of a Modernized Passenger Coach for Multimodal Transport: Effect of Wheel Wear and Clearance Optimization. *Future Transp.* **2025**, *5*, 168. [CrossRef]
31. Pawlik, M. Rail Transport Systems Safety, Security and Cybersecurity Functional Integrity Levels. In *Research Methods and Solutions to Current Transport Problems. ISCT21 2019*; Siergiejczyk, M., Krzykowska, K., Eds.; Advances in Intelligent Systems and Computing; Springer: Cham, Switzerland, 2020; Volume 1032. [CrossRef]
32. Baranovska, O.; Bulakh, M. Safety management of transport systems. *Sci. Technol. Innov.* **2025**, *22*, 24–30. [CrossRef]
33. Bondarenko, I.; Campisi, T.; Tesoriere, G.; Neduzha, L. Using Detailing Concept to Assess Railway Functional Safety. *Sustainability* **2023**, *15*, 18. [CrossRef]
34. Tudor, I.A.; Gîrbacia, F. Mapping Research Trends in Road Safety: A Topic Modeling Perspective. *Vehicles* **2026**, *8*, 69. [CrossRef]
35. Wojciechowski, H.; Michalak, D.; Merkisz, J. Differences in structural design and safety requirements of urban buses in Europe and North America. *Combust. Engines* **2026**, *206*, 130–139. [CrossRef]
36. Xu, S.; Wen, H.; Zhao, S. Beyond Structural Adjustment: Quantifying the Dominance of New Energy Vehicles in Expressway Carbon Mitigation Targets. *Vehicles* **2026**, *8*, 118. [CrossRef]
37. Sulym, A.O.; Khozia, P.O.; Fomin, O.V.; Bahrov, O.M. Management of Energy Exchange Process on Subway cars with On-Board Capacitive Energy Storage. *Probl. Energ. Reg.* **2025**, *1*, 49–63. [CrossRef]
38. Sulym, A.; Khozia, P.; Fomin, O.; Khara, M.; Burlutskyy, O. New approach to determining the rational parameters of the on-board capacitive energy storage for metro train. In Proceedings of the 27th International Scientific Conference Transport Means, Palanga, Lithuania, 4–6 October 2023; pp. 733–738.
39. Burnete, N.V.; Mariașiu, F.; Iclodean, C. Intelligent Mobility and Sustainable Automotive Technologies. *Vehicles* **2026**, *8*, 156. [CrossRef]
40. Kalivoda, J.; Neduzha, L. Running Dynamics of Rail Vehicles. *Energies* **2022**, *15*, 5843. [CrossRef]

41. Fedosov-Nikonov, D.V.; Sulym, A.O.; Ilchyshyn, V.V.; Safronov, O.M.; Kelrikh, M.B. Study of strength characteristics of the long wheelbase flat cars. *IOP Conf. Ser. Mater. Sci. Eng.* **2020**, *985*, 012029. [CrossRef]
42. Jiang, H.; Xie, Y.; Li, A.; Tang, B. Geometry–Dynamics Coupled Lateral Control with Adaptive Speed Planning for Six-Axle Vehicles Under Confined Spatial and Low-Friction Conditions Based on Dual-Point Preview and Multi-Mode Steering Fusion. *Actuators* **2026**, *15*, 363. [CrossRef]
43. Oszczypała, M.; Ziółkowski, J.; Małachowski, J. Modelling the Operation Process of Light Utility Vehicles in Transport Systems Using Monte Carlo Simulation and Semi-Markov Approach. *Energies* **2023**, *16*, 2210. [CrossRef]
44. Lageweg, S.; Fabiś, P. Analysis of Dynamic Parameters of Electric and Combustion Vehicles. *Energies* **2026**, *19*, 1256. [CrossRef]
45. Zhang, P.; Yi, W.; Song, Y.; Wu, P.; Chan, A.P.C.; Gao, Y. Spatiotemporal Particle Swarm Optimization for Future Cost Allocation in Large-Scale Transportation Infrastructure Maintenance. *ISPRS Int. J. Geo-Inf.* **2026**, *15*, 70. [CrossRef]
46. Paulauskas, V.; Paulauskas, D.; Paulauskas, V. Achieving Port Sustainability by Harnessing the Potential of Port Operations, Ships and Tugboats. *Sustainability* **2026**, *18*, 1916. [CrossRef]
47. Lelisa Dirirsa, S.; Gao, Y.; Raza, M.; Shrestha, R.; He, Q. Planning and Design of an Integrated Railway-Highway Infrastructure: A Review. *J. Transp. Eng. Part A Syst.* **2025**, *151*, 6. [CrossRef]
48. Khanmohamadi, M.; Guerrieri, M. Towards Transportation Metaverse: A Conceptual Perspective on Future Road, Railway, Maritime, and Aviation Systems. *Infrastructures* **2026**, *11*, 181. [CrossRef]
49. Korendiy, V.; Krot, P.; Kachur, O.; Gurskyi, V. Analyzing the Locomotion Conditions of a Wheeled Vibration-Driven System with a V-Shaped Suspension. In *Advances in Design, Simulation and Manufacturing VII. DSMIE 2024*; Ivanov, V., Pavlenko, I., Edl, M., Machado, J., Xu, J., Eds.; Lecture Notes in Mechanical Engineering; Springer: Cham, Switzerland, 2024. [CrossRef]
50. Jagelčák, J.; Kubáňová, J.; Zdanowicz, P.; Tkaczyk, S. Impact assessment of the transported load mass on the lateral dynamics of a light delivery vehicles. *Sci. Rep.* **2026**, *16*, 6653. [CrossRef]
51. Kojis, P.; Danilevičius, A.; Šabanovič, E.; Skrickij, V. The Second Generation of Electric Vehicles: Integrated Corner Solutions. In *TRANSBALTICA XII: Transportation Science and Technology. TRANSBALTICA 2021*; Prentkovskis, O., Yatskiv (Jackiva), I., Skačkauskas, P., Junevičius, R., Maruschak, P., Eds.; Lecture Notes in Intelligent Transportation and Infrastructure; Springer: Cham, Switzerland, 2022. [CrossRef]
52. Sulym, A.; Pavlenko, Y.; Fedosov-Nikonov, D.; Popova, T.; Dižo, J.; Blatnický, M. Study of Dynamics of Corrosive Wear of Load-Bearing Metal Structures of Subway Cars with Expired Service Life. *Appl. Sci.* **2026**, *16*, 1631. [CrossRef]
53. Paluch, M.; Noga, M. Influence of hydrogen addition on performance and ecological parameters of a spark-ignition internal combustion engine at part load typical for urban traffic. *Adv. Sci. Technol. Res. J.* **2025**, *19*, 262–270. [CrossRef]
54. Naik, B.; Eustace, D. Emerging Transportation Safety and Operations: Practical Perspectives. *Vehicles* **2026**, *8*, 180. [CrossRef]
55. Guadagno, M.; Berzi, L.; Pierini, M.; Delogu, M. Modeling and Simulation of Active Suspension System for Road Vehicles and Sensitivity to Design Criteria for Energy Efficiency. *Eng. Proc.* **2026**, *131*, 17. [CrossRef]
56. Hu, Z.; Mo, S.; Liu, H.; Mo, F. Optimizing Vehicle Body Cross-Sections Using a Parametric Mathematical Model. *Appl. Sci.* **2024**, *14*, 11427. [CrossRef]
57. Ki, W.-Y.; Heo, S.-J.; Kang, D.-O.; Yim, H.J.; Lee, K.W.; Kim, J.H.; Lee, C.K. Development of knowledge-based body structure concept design model. *Int. J. Automot. Technol.* **2017**, *18*, 429–437. [CrossRef]
58. Hou, W.B.; Shan, C.L.; Zhang, H.Z. Asme Multi-level optimization method for vehicle body in conceptual design. In Proceedings of the ASME International Design Engineering Technical Conferences and Computers and Information in Engineering Conference, Boston, MA, USA, 2–5 August 2015. [CrossRef]
59. Fard, M.; Yao, J.; Taube, R.; Davy, J.L. The concept modeling method: An approach to optimize the structural dynamics of a vehicle body. *Proc. Inst. Mech. Eng. Part D J. Automob. Eng.* **2020**, *234*, 2923–2932. [CrossRef]
60. Aulig, N.; Nutwell, E.; Menzel, S.; Detwiler, D. Preference-based topology optimization for vehicle concept design with concurrent static and crash load cases. *Struct. Multidiscip. Optim.* **2017**, *57*, 251–266. [CrossRef]
61. Tullah, M.H.; Sumarsono, D.A.; Susanto, I.; Zainuri, F.; Prasetya, S.; Noval, R.; Permana, S.; Aprianto, B.D. Design and evaluation of hollow frame structures for the development of urban-centric two-passenger electric vehicles. *East.-Eur. J. Enterp. Technol.* **2023**, *5*, 80–86. [CrossRef]
62. Walczak, B.; Dao, P.B.; Malaca, P.; Michalak, D.; Staszewski, W.J. Development of Virtual Electric Bus Superstructure Model Including Fatigue Load Spectra and Crashworthiness. *Processes* **2026**, *14*, 2096. [CrossRef]
63. Kepka, M.; Volak, J.; Minich, R.; Martinu, M.; Pavlata, P.; Dopierala, L.; Walczak, B. Experiments to Support the Improvement of the Integrity and Resistance of the Bus Bodywork in a Rollover Accident. *Procedia Struct. Integr.* **2023**, *47*, 113–118. [CrossRef]
64. Lu, C.; Zeng, F. Analysis and optimization of bus body structure. *J. Phys. Conf. Ser.* **2025**, *3021*, 012048. [CrossRef]
65. Niewczas, A.; Rymarz, J.; Ślęzak, M.; Kasperek, D.; Hołyszko, P. Reliability Study of Electric Buses in the Urban Public Transport System. *Energies* **2025**, *18*, 3863. [CrossRef]
66. Yang, J.; Xing, S.; Chen, Y.; Qiu, R.; Hua, C.; Dong, D. An Evaluation Model for the Comfort of Vehicle Intelligent Cockpits Based on Passenger Experience. *Sustainability* **2022**, *14*, 6827. [CrossRef]

67. Gao, F.; Ge, X.; Li, J.; Fan, Y.; Li, Y.; Zhao, R. Intelligent Cockpits for Connected Vehicles: Taxonomy, Architecture, Interaction Technologies, and Future Directions. *Sensors* **2024**, *24*, 5172. [CrossRef]
68. Yuan, Q.; Tan, Y.; Ma, N.; Guo, J. Intelligent Cockpit Technology Brings About a Revolution in Automotive Ergonomics. In *Man-Machine-Environment System Engineering. MMESE 2025*; Long, S., Dhillon, B.S., Ye, L., Eds.; Lecture Notes in Electrical Engineering; Springer: Singapore, 2026; Volume 1477. [CrossRef]
69. Ruban, D.; Kraynyk, L.; Ruban, H.; Zakharova, M.; Metelap, V.; Khotunov, V.; Mykhaylyuta, S. Devising an approach to assessing the durability of bus body on a frame chassis. *East.-Eur. J. Enterp. Technol.* **2023**, *2*, 32–39. [CrossRef]
70. Capata, R.; Martellucci, L.; Buccolini, D.; De Felice, C.; Giannini, M. Validation Method of Torsional Stiffness for a Single-Seater Car Chassis. *World Electr. Veh. J.* **2025**, *16*, 604. [CrossRef]
71. Knotz, C.; Sölkner, T.; Wernig, J.; Klink, J.; Haas, M.; Vögl, R.; Hauptmann, T. Challenges of Passenger Cars. In *Systems Engineering for Automotive Powertrain Development*; Hick, H., Küpper, K., Sorger, H., Eds.; Springer: Cham, Switzerland, 2020. [CrossRef]
72. Hyttinen, J.; Wentzel, H.; Österlöf, R.; Jerrelind, J.; Drugge, L. Development and Analysis of an On-Road Torque Measurement Device for Trucks. *Exp. Mech.* **2024**, *64*, 455–466. [CrossRef]
73. Karaskova, J.; Sliva, A.; Nainaragaram Ramasamy, M.; Olivkova, I.; Besta, P.; Dizo, J. Optimizing Calibration Processes in Automotive Component Manufacturing. *Systems* **2026**, *14*, 92. [CrossRef]
74. Holenko, K.; Dykha, O.; Piętocha, A.; Kernytskyy, I.; Horbay, O.; Górski, W.; Koda, E. Side-Impact Crashworthiness of Low-Emission Electric Bus with Battery-Integrated Inter-Window Pillars Under UNECE R95 Conditions. *Machines* **2026**, *14*, 703. [CrossRef]
75. Dąbrowski, F.; Grzejszczyk, Z.; Rzymkowski, C.; Wiśniewski, P. Frontal Impact Energy Absorbers for Passenger Cars. *Sensors* **2024**, *24*, 6563. [CrossRef]
76. Poliak, M.; Frej, D.; Jaśkiewicz, M.; Caban, J.; Górniak, A.; Gidlewski, M.; Hajduk, I.E.; Kubiak, P.; Tarnapowicz, D. Analysis of Head Movement in KPSIT Dummies and the Impact of Seats and Seat Belts during Low-Speed Collisions 20 km/h. *Sensors* **2024**, *24*, 5714. [CrossRef]
77. Dumitrache, A.-M.; Dumitrache, I.-A.; Iozsa, D.; Molea, A. Experimental and Numerical Impact Assessment of a Heavy-Duty Truck Cab Reconstructed from 3D Scanning According to the Swedish VVFS 2003:29 Procedure. *Eng* **2026**, *7*, 137. [CrossRef]
78. Kilikevičius, A.; Pravilonis, T.; Matijošius, J.; Sokolovskij, E.; Kilikevičienė, K.; Vainorius, D. The Impact of Vibrations and Transport Systems on Human Comfort and Health: A Perspective on the Development of Sustainable City Buses. *Sustainability* **2025**, *17*, 10258. [CrossRef]
79. Pravilonis, T.; Sokolovskij, E.; Kilikevičius, A.; Matijošius, J.; Kilikevičienė, K. The Usage of Alternative Materials to Optimize Bus Frame Structure. *Symmetry* **2020**, *12*, 1010. [CrossRef]
80. Kniaziev, S.; Guerrieri, M.; Kniazieva, H.; Trembach, B.; Babyak, M.; Neduzha, L. Development of a Base Material–Barrier Coating System Using Affordable Raw Materials for the Sustainable Production of Critical Railway Components. *Sustainability* **2026**, *18*, 4512. [CrossRef]
81. An, T.T.; Tuan, N.V. Passenger bus vibration analysis with optimized parameters under diverse operating conditions. *Proc. Inst. Mech. Eng. Part D J. Automob. Eng.* **2026**, 09544070261447794. [CrossRef]
82. He, Y.; Shepherd, P.; Wang, J. Layout Optimisation of Frame Structures with Multiple Constraints and Geometric Complexity Control. *Appl. Sci.* **2024**, *14*, 8157. [CrossRef]
83. Yao, R.; Pang, T.; Zhang, B.; Fang, J.; Li, Q.; Sun, G. On the crashworthiness of thin-walled multi-cell structures and materials: State of the art and prospects. *Thin-Walled Struct.* **2023**, *189*, 110734. [CrossRef]
84. Haryanto, I.; Raharjo, F.A.; Kurdi, O.; Haryadi, G.D. Optimization of Bus Body Frame Structure for Weight Minimizing with Constraint of Natural Frequency using Adaptive Single-Objective Method. *Int. J. Sustain. Transp. Technol.* **2018**, *1*, 9–14. [CrossRef]
85. Wang, T.; Shao, X.; Qin, D.; Huang, K.; Yao, M.; Duan, Y. An Adaptive GPR-Based Multidisciplinary Design Optimization of Structural and Control Parameters of Intelligent Bus for Rollover Stability. *Mathematics* **2025**, *13*, 782. [CrossRef]
86. Wang, P.; Bai, Y.; Fu, C.; Lin, C. Lightweight design of an electric bus body structure with analytical target cascading. *Front. Mech. Eng.* **2023**, *18*, 2. [CrossRef]
87. Yi, P.; Wong, S.V.; Han, Y.; Ahmad, b.Y.; Tan, K.S.; As'arry, A.; Zhang, S.; Ren, P. Crashworthiness Research Based on Lightweight Bus of Honeycomb Sandwich Body. *J. Eng.* **2025**, *2025*, 8829522. [CrossRef]
88. Kongwat, S.; Jongpradist, P.; Hasegawa, H. Lightweight Bus Body Design and Optimization for Rollover Crashworthiness. *Int. J. Automot. Technol.* **2020**, *21*, 981–991. [CrossRef]
89. Liu, Q.; Lin, Y.; Zong, Z.; Sun, G.; Li, Q. Lightweight design of carbon twill weave fabric composite body structure for electric vehicle. *Compos. Struct.* **2013**, *97*, 231–238. [CrossRef]
90. Yao, C.; Yang, M. Research on lightweight design and finite element analysis of a 9 meter bus body frame. *J. Phys. Conf. Ser.* **2021**, *1748*, 062022. [CrossRef]
91. Wang, D.; Xie, C.; Liu, Y. Multi-objective collaborative optimization for the lightweight design of an electric bus body frame. *Automot. Innov.* **2020**, *3*, 250–259. [CrossRef]

92. Holenko, K.; Dykha, O.; Dyka, M.; Makovkin, O.; Horbay, O. Application of Catenary Curve Principles in the Design of the Low-Floor Bus Body Cross-Section. In *Advances in Design, Simulation and Manufacturing VIII. DSMIE 2025*; Campilho, R.D., Ivanov, V., Pinto, G.F., Baptista, A., Silva, F.J.G., Eds.; Lecture Notes in Mechanical Engineering; Springer: Cham, Switzerland, 2025; pp. 37–46. [CrossRef]
93. Lopes, R.; Viriato, N.; Cunha, R.; Maia, R.; Rodrigues, R.; Parente, M.; Moreira, P. Passive safety solutions on coach according ECE R29: Experimental and numerical analyses. *Procedia Struct. Integr.* **2023**, *42*, 1159–1168. [CrossRef]
94. Yao, C.; Yang, M. Analysis of strength stiffness and modes for bus body frame. *J. Phys. Conf. Ser.* **2021**, *1748*, 062073. [CrossRef]
95. Holenko, K.; Dykha, O.; Dykha, M.; Dytyniuk, V.; Horbay, O.; Voichyshyn, Y.; Krainyk, L. Determining the effect of triangular interwindow openings in a bus body on its structure, strength and passive safety. *East.-Eur. J. Enterp. Technol.* **2025**, *1*, 50–63. [CrossRef]
96. Ruban, D.; Kraynyk, L.; Ruban, H.; Hrubel, M.; Duzhyi, R.; Babaryha, A. Development of technological principles of technical control of bus bodies during operation based on passive safety conditions. *East.-Eur. J. Enterp. Technol.* **2022**, *6*, 91–100. [CrossRef]
97. Nguyen, T.C. Research to Evaluate the Quality of Passenger Bus Body Frame, Assuring the Passive Safety in the Design Process. *Appl. Mech. Mater.* **2019**, *889*, 440–447. [CrossRef]
98. Sordi, A.; Menino, B.G.; Isoton Pistorello, G.; do Nascimento, V.; Telli, G.D. Performance of Electric Bus Batteries in Rollover Scenarios According to ECE R66 and R100 Standards. *World Electr. Veh. J.* **2025**, *16*, 528. [CrossRef]
99. Ruban, D.; Kraynyk, L.; Ruban, H.; Sosyk, A.; Shcherbyna, A.; Dudarenko, O.; Artyukh, A. Forecasting the durability of public transport bus bodies depending on operating conditions. *East.-Eur. J. Enterp. Technol.* **2021**, *4*, 26–33. [CrossRef]
100. El-Basiouny, A.M.; Askar, H.S.; El-Zoughiby, M.E. Effect of compression pre-force and web openings on torsional strength of UHPC hollow beams using numerical and mathematical modeling. *Sci. Rep.* **2025**, *15*, 25880. [CrossRef]
101. Qin, P.; Shi, Y.; Huang, J.; Lu, J.; Tu, W.; Wu, H. Parametric Cross-Section Design and Crashworthiness Optimization of High-Strength Steel Double-Cell Roll-Formed Tubes Under Lateral Bending. *World Electr. Veh. J.* **2026**, *17*, 179. [CrossRef]
102. Magalhães, K.M.M.; Brasil, R.M.L.R.F.; Wahrhaftig, A.M.; Siqueira, G.H.; Bondarenko, I.; Neduzha, L. Influence of Atmospheric Humidity on the Critical Buckling Load of Reinforced Concrete Columns. *Int. J. Struct. Stab. Dyn.* **2022**, *22*, 2250011. [CrossRef]
103. Liu, Y.; Gao, X.; Li, W.; Tan, J. Design and finite element analysis of new energy bus body frame. *Front. Mech. Eng.* **2026**, *12*, 1775256. [CrossRef]
104. Muresanu, A.D.; Dudescu, M.C.; Tica, D. Study on the Crashworthiness of a Battery Frame Design for an Electric Vehicle Using FEM. *World Electr. Veh. J.* **2024**, *15*, 534. [CrossRef]
105. Holenko, K.; Koda, E.; Dykha, O.; Kernytskyy, I.; Horbay, O.; Chalecki, M.; Royko, Y.; Humeniuk, R.; Sharybura, A.; Sholudko, Y.; et al. Evaluation of Influence of the Integrated Welded Handrail System in the Bus Body Frame on Strength and Passive Safety. *Appl. Sci.* **2026**, *16*, 3039. [CrossRef]
106. Trembach, B.; Dmitriiev, O.; Kulahin, K.; Balenko, O.; Maliuha, V.; Neduzha, L. Hybrid Optimization of Hardfacing Conditions and the Content of Exothermic Additions in the Core Filler During the Flux-Cored Arc Welding Process. *Eng* **2026**, *7*, 23. [CrossRef]
107. Trembach, B.; Krbata, M.; Haibadulov, B.; Iokhov, O.; Tsebriuk, I.; Pomohaiev, I.; Korobkov, Y.; Neduzha, L. Optimisation of Elemental Transfer Efficiency in Fe-C-Cr-Ti-Cu Hardfacing by Self-Shielded Flux-Cored Wire: A Synergistic Taguchi–ANOVA–FD–PCA–GRA Approach. *Eng* **2026**, *7*, 139. [CrossRef]
108. Shi, Y.; Liu, X.; Chang, Y.; Chen, J.; Zhang, D.; Kuang, Y. Machine Learning-Based Method for Predicting the Mechanical Response of Prestressed Cable Tensioning in Aqueduct Structures. *Buildings* **2026**, *16*, 1624. [CrossRef]
109. Kepka, M.; Kepka, M.; Minich, R.; Vaclavik, J. Service load analyses for fatigue life calculations and laboratory tests of welded joints of trolleybus bodyworks. *Procedia Struct. Integr.* **2026**, *77*, 272–278. [CrossRef]
110. Holenko, K.; Dykha, O.; Koda, E.; Kernytskyy, I.; Horbay, O.; Royko, Y.; Fornalchyk, Y.; Berezovetska, O.; Rys, V.; Humenuyk, R.; et al. Structure and Strength Optimization of the Bogdan ERCV27 Electric Garbage Truck Spatial Frame Under Static Loading. *Appl. Sci.* **2024**, *14*, 11012. [CrossRef]
111. Holenko, K.; Dykha, O.; Koda, E.; Kernytskyy, I.; Horbay, O.; Royko, Y.; Humeniuk, R.; Sholudko, Y.; Rys, V.; Berezovetskyi, S.; et al. Peculiarities of Assessing Body Strength When Converting a Bus from Diesel to Electric Traction Following the UNECE R100 Regulation. *Appl. Sci.* **2025**, *15*, 8115. [CrossRef]
112. Gao, X.; Shang, J.; Song, Y. Mechanical behavior of single concrete frame strengthened with externally prestressed cables. *PLoS ONE* **2026**, *21*, e0350097. [CrossRef]
113. Wang, X.; Yin, Z.; Ma, J.; Qin, W.; Yang, Y.; Li, P. Numerical and Theoretical Investigation into the Global Stability Behaviour of Glulam Gridshells Stiffened by Prestressed Cables. *Buildings* **2026**, *16*, 693. [CrossRef]
114. Li, M.; Song, F.; Liu, H.; Li, J. Mechanism of Fatigue Fracture of Fork-Eye Anchor Heads Induced by Excessive Vibration of Stay Cables in Landscape Cable-Stayed Bridges. *Buildings* **2026**, *16*, 3045. [CrossRef]
115. Wu, K.; Wang, L.; Ge, W.; Shu, H.; Liu, Y.; Chen, K. Research on Vehicle–Bridge-Coupled Vibration of Multi-Tower High-Pier Partially Cable-Stayed Bridge Based on a Single Vehicle. *Buildings* **2025**, *15*, 2865. [CrossRef]

116. He, X.; Wang, Z.; Li, C.; Gao, C.; Liu, Y.; Li, C.; Liu, B. Experimental Test and Finite Element Analysis on a Concrete Box Girder of a Cable-Stayed Bridge with W-Shaped Prestressed Concrete Diagonal Braces. *Buildings* **2024**, *14*, 506. [CrossRef]
117. Zhang, Q.; Liu, Z.; Gao, S.; Liu, Z.; Meng, X.; Zhang, G.; Lu, B.; Lu, Y. Linearization of Power Flow Model for Asymmetrically Coupled Electrified Railway-grid Hybrid System. *J. Power Energy Syst.* **2026**, *12*, 4. [CrossRef]
118. Wang, Z.; Tao, Y.; Zhang, S.; Liu, X.; Lin, Y.; Li, L.; Tan, J.; Li, Z. Spatial Spiral Tube Multi-Roller Bending: Accurate Axial Prediction Utilizing Awpso-Fecam-Lstm Framework. *Expert Syst. Appl.* **2026**, *296*, 128960. [CrossRef]
119. Zhang, F.; Mehdi, A.I.; Kim, M.-Y. LTB analysis of pre-stressed steel beams using mono-symmetric thin-walled beam and spatially inclined un-bonded cable elements. *Thin-Walled Struct.* **2023**, *191*, 111050. [CrossRef]
120. Wadee, M.A.; Hadjipantelis, N.; Gardner, L.; Lozano-Galant, J.A. Stability of steel struts with externally anchored prestressed cables. *J. Constr. Steel Res.* **2020**, *164*, 105790. [CrossRef]
121. Habibi, T.; Rhode-Barbarigos, L.; Keller, T. Effects of prestress implementation on self-stress state in large-scale tensegrity structure. *Eng. Struct.* **2023**, *288*, 116222. [CrossRef]
122. Panda, P.N.; Chakrabarti, A.; Prakash, V. Performance of Steel Buildings with Pretensioned Steel Cable Braces under Seismic Loading. *J. Struct. Des. Constr. Pract.* **2025**, *30*, 04025009. [CrossRef]
123. Li, J.; Feng, D. Fatigue life evaluation of bridge stay cables subject to monitoring traffic and considering road roughness. *Eng. Struct.* **2023**, *293*, 116572. [CrossRef]
124. Yan, C.; Liu, C.; Yu, S. Fatigue life prediction of stay cables under vehicle load considering corrosion variability. *Structures* **2023**, *56*, 104879. [CrossRef]
125. Shen, G.; Coules, H.; Macdonald, J. Bending fatigue performance of high-strength seven-wire monostrand. *Eng. Struct.* **2024**, *301*, 117291. [CrossRef]
126. Behera, A.; Kumari, R.; Porter, G.A.; Sahoo, P.; Davim, J.P. (Eds.) *Advances in Materials Processing for Industry 5.0*; Lecture Notes on Multidisciplinary Industrial Engineering; Springer: Berlin/Heidelberg, Germany, 2026.
127. Kilikevičius, A.; Kilikevičienė, K.; Fursenko, A.; Matijošius, J. The Analysis of Vibration Signals of Critical Points of the Bus Body Frame. *Period. Polytech. Transp. Eng.* **2020**, *48*, 296–304. [CrossRef]
128. Stan, C.; Oprea, R.A. Vibration Comfort Assessment Methods in Heavy Vehicles: Models, Standards and Numerical Approaches—A State-of-the-Art Review. *Technologies* **2026**, *14*, 98. [CrossRef]
129. Konieczny, L.; Fabis, P.; Matijošius, J.; Duda, K.; Deuszkiewicz, P.; Kilikevičius, A. Analysis of the Impact of Vibrations on the Driver of a Motor Vehicle. *Appl. Sci.* **2025**, *15*, 5510. [CrossRef]

Disclaimer/Publisher's Note: The statements, opinions and data contained in all publications are solely those of the individual author(s) and contributor(s) and not of MDPI and/or the editor(s). MDPI and/or the editor(s) disclaim responsibility for any injury to people or property resulting from any ideas, methods, instructions or products referred to in the content.